Journal of Materials Chemistry A

Colloidal Ni-Co-Sn Nanoparticles as Efficient Electrocatalysts for the Methanol Oxidation Reaction

Journal:	*Journal of Materials Chemistry A*
Manuscript ID	TA-ART-08-2018-008242
Article Type:	Paper
Date Submitted by the Author:	24-Aug-2018

Complete List of Authors:	Li, Junshan; Institut de Recerca en Energia de Catalunya, Luo, Zhishan; IREC, He, Feng; Key Laboratory of Organic Solids, Institute of Chemistry, Chinese Academy of Sciences Zuo, Yong; Institut de Recerca en Energia de Catalunya Liu, Junfeng; Catalonia Institute for Energy Research, Advanced Materials Du, Ruifeng; China University of Geosciences, Yu, Xiaoting; Catalonia Institute for Energy Research (IREC) Zhang, Ting; Catalan Institute of Nanoscience and Nanotechnology Tang, Pengyi; Catalan Institute of Nanoscience and Nanotechnology (ICN2), F. Infante Carrió, Maria; Catalan Institute of Nanoscience and Nanotechnology, Arbiol, Jordi; Institut Català de Nanociència i Nanotecnologia (ICN2), CSIC and The Barcelona Institute of Science and Technology (BIST), Advanced Electron Nanoscopy (GAeN); ICREA, Llorca, Jordi; Technical University of Catalonia, Institute of Energy Technologies Cabot, Andreu; Catalonia Institute for Energy Research, Advanced Materials

Institut de Recerca en Energia de Catalunya
Catalonia Institute for Energy Research

Advanced Materials Research Area
Functional Nanomaterials Group
Jardi de les Dones de Negre 1
08930, Sant Adria del Besos, Barcelona (Spain)
Tel. +34 93 403 9154
Fax +34 93 402 11 48

Journal of Materials Chemistry A August 24th, 2018

Dear Editor,

We are electronically submitting for your consideration as a potential contribution in **Journal of Materials Chemistry A** manuscript entitled "**Colloidal Ni-Co-Sn Nanoparticles as Efficient Electrocatalysts for the Methanol Oxidation Reaction**" Junshan Li, Zhishan Luo, Feng He, Yong Zuo, Junfeng Liu, Xiaoting Yu, Ruifeng Du, Ting Zhang, Maria F. Infante-Carrió, Pengyi Tang, Jordi Arbiol, Jordi Llorca and Andreu Cabot. This work has not been published previously, nor is it under consideration elsewhere.

The deployment of direct methanol fuel cells requires the design and engineering of cost-effective and durable electrocatalyst for the methanol oxidation reaction (MOR). As an alternative to noble metals, Ni-based alloys have shown excellent performance and good stability toward MOR. Herein, we present a series of $Ni_{3-x}Co_xSn_2$ colloidal nanoparticles (NPs) with composition tuned over the entire range ($0 \leq x \leq 3$). We demonstrate electrodes based on these ternary NPs to provide improved catalytic performance toward MOR in alkaline medium when compared with binary Ni_3Sn_2 NPs. A preliminary composition optimization resulted in $Ni_{2.5}Co_{0.5}Sn_2$ NP-based electrodes exhibiting extraordinary mass current densities, up to 1050 mA mg^{-1}, at 0.6 V *vs.* Hg/HgO in 1.0 M KOH containing 1.0 M methanol. This current density was about a two-fold larger than that of Ni_3Sn_2 electrodes (563 mA mg^{-1}). This excellent performance was associated with an increase of the surface overage of active species and an enhancement of the diffusivity of the reaction limiting species with the substitution of small amounts of Ni by Co. Additionally, saturation of the catalytic activity at higher methanol concentrations was measured for $Ni_{3-x}Co_xSn_2$ NP-based electrodes containing a small amount of Co when compared with binary Ni_3Sn_2 NPs. While the introduction of small amounts of Co improved the activity toward MOR, a slight decrease of the catalyst durability with the Co introduction was obtained. Additional density functional theory calculations on metal alloy surfaces showed the incorporation of Co within the Ni_3Sn_2 structure to provide more effective sites for CO and CH_3OH adsorption. However, the relatively lower stability could not be related with CO or CH_3OH poisoning.

Thank you for your consideration of this manuscript.

Sincerely,

Prof. Andreu Cabot
Advanced Material Research Department
Catalonia Institute for Energy Research - IREC
Phone: +34 625615115
acabot@irec.cat

Journal Name

ARTICLE

Colloidal Ni-Co-Sn Nanoparticles as Efficient Electrocatalysts for the Methanol Oxidation Reaction

Received 00th January 20xx,
Accepted 00th January 20xx

DOI: 10.1039/x0xx00000x

www.rsc.org/

Junshan Li,[a,b] Zhishan Luo,[a,*] Feng He,[c,d,*] Yong Zuo,[a,b] Junfeng Liu,[a,b] Xiaoting Yu,[a,b] Ruifeng Du,[a,b] Ting Zhang,[e] Maria F. Infante-Carrió,[e] Pengyi Tang,[e] Jordi Arbiol,[e,f] Jordi Llorca,[g] Andreu Cabot [a, f,*]

The deployment of direct methanol fuel cells requires the design and engineering of cost-effective and durable electrocatalyst for the methanol oxidation reaction (MOR). As an alternative to noble metals, Ni-based alloys have shown excellent performance and good stability toward MOR. Herein, we present a series of $Ni_{3-x}Co_xSn_2$ colloidal nanoparticles (NPs) with composition tuned over the entire range ($0 \le x \le 3$). We demonstrate electrodes based on these ternary NPs to provide improved catalytic performance toward MOR in alkaline medium when compared with binary Ni_3Sn_2 NPs. A preliminary composition optimization resulted in $Ni_{2.5}Co_{0.5}Sn_2$ NP-based electrodes exhibiting extraordinary mass current densities, up to 1050 mA mg^{-1}, at 0.6 V *vs.* Hg/HgO in 1.0 M KOH containing 1.0 M methanol. This current density was about a two-fold larger than that of Ni_3Sn_2 electrodes (563 mA mg^{-1}). This excellent performance was associated with an increase of the surface overage of active species and an enhancement of the diffusivity of the reaction limiting species with the substitution of small amounts of Ni by Co. Additionally, saturation of the catalytic activity at higher methanol concentrations was measured for $Ni_{3-x}Co_xSn_2$ NP-based electrodes containing a small amount of Co when compared with binary Ni_3Sn_2 NPs. Additional density functional theory calculations on metal alloy surfaces showed the incorporation of Co within the Ni_3Sn_2 structure to provide more effective sites for CO and CH_3OH adsorption. However, the relatively lower stability could not be related with CO or CH_3OH poisoning.

Introduction

The development of renewable energy technologies able to reduce the use of fossil fuels is one of the biggest challenges we face this 21st century. To this end, direct alcohol fuel cells able to convert chemical energy stored in alcohols into electricity, are regarded as a very promising energy conversion technology.[1–9] More particularly, direct methanol fuel cells (DMFCs) provide several advantages, including high energy density, high efficiency, low emissions, fast mechanical refueling and simple operation.[10–13] In addition, methanol not only provides a high energy density, but also an easy storage and distribution, which makes it one of the most interesting fuels.[10,14] In this scenario, the development of electrocatalyst for the methanol oxidation reaction (MOR) has become a very dynamic research field.[12,15]

State-of-the-art electrocatalysts for MOR are generally based on noble metals and their alloy, e.g. Pt,[16–21] PtNi,[22–28] PtCo,[29–31] PuCu,[32,33] PtPd,[34,35] and PtSn[36–40] etc. However, the low tolerance to CO and the high cost and scarcity of these materials have strongly limited the commercialization of DMFCs.[13,41–43] Therefore, over the past years, researchers have devoted increasing attention in searching for alternative earth abundant and cost-efficient MOR electrocatalysts.

While no single metal has provided electrocatalytic properties comparable to Pt and Pt-group metals, particular bimetallic compositions have demonstrated very promising performances and stabilities. Among the earth-abundant elements, the most promising MOR catalysts under alkaline condition are bimetallic alloys based on Ni, e.g. Ni-Cu,[41,44–46] Ni-Mn,[47] Ni-Fe,[48,49] Ni-Co,[50–57] Ni-Sn.[58] In a previous study, we demonstrated NiSn NPs to present outstanding performance for electrocatalytically MOR in alkaline medium, and particularly an enhanced stability compared with state-of-the-art elemental Ni NPs.[58]

A main advantage of bimetallic catalysts over elemental compositions is their offering of additional degrees of freedom to control the surface electronic structure, to provide optimum active

a Catalonia Institute for Energy Research - IREC, Sant Adrià del Besòs, Barcelona, 08930, Spain
b Departament d'Electronica, Universitat de Barcelona, 08028 Barcelona, Spain
c Key Laboratory of Organic Solids, Institute of Chemistry, Chinese Academy of Sciences, Beijing 100190, PR China.
d University of Chinese Academy of Sciences, Beijing 100049, P.R. China.
e Catalan Institute of Nanoscience and Nanotechnology (ICN2), CSIC and BIST, Campus UAB, Bellaterra, 08193 Barcelona, Spain
f ICREA, Pg. Lluís Companys 23, 08010 Barcelona, Spain
g Institute of Energy Technologies, Department of Chemical Engineering and Barcelona Research Center in Multiscale Science and Engineering. Universitat Politècnica de Catalunya, EEBE, 08019 Barcelona, Spain

Corresponding Author
* Andreu Cabot: acabot@irec.cat
* Zhishan Luo: luozs@mail.sustc.edu.cn
* Feng He: hefeng2018@iccas.ac.cn
Electronic Supplementary Information (ESI) available: additional SEM-EDS, TEM, HRTEM, XPS, FT-IR, electrochemical characterizations and DFT calculations.
See DOI: 10.1039/x0xx00000x

sites for one or various concatenated catalytic reaction, and to improve stability by combined catalytic reactions.[9,59–61] In the same direction, ternary compositions provide even larger oportunities to optimize electronic properties and provide suitable active sites for one or multiple reactions. However, few ternary alloy catalysts have been reported toward MOR and other electrocatalytic reactions. This is in large part due to the difficulty of producing ternary alloys with controlled composition. As an example, Hamza and coworkers demonstrated ternary oxide electrocatalysts $CuCoNiO_x$ supported on carbon nanotubes to have a notable activity toward MOR.[62] Recently, Rostami et al. demonstrated that NiCuCo on graphite electrodes enhanced activity and stability towards MOR.[53] However, in none of these previous works the full potential of ternary compositions to optimize catalytic properties could be demonstrated because no composition adjustment was attempted.

In this work, we detail a procedure to produce ternary $Ni_{3-x}Co_xSn_2$ NPs with tuned composition in all the Ni:Co ratio range ($0 \le x \le 3$). Subsequently, these NPs are supported on carbon black and tested as electrocatalysts toward MOR.

Experimental

Chemicals: Nickel(II) acetylacetonate ($Ni(acac)_2 \cdot xH_2O$ (x~2), 95%, Sigma-Aldrich), cobalt(II) acetylacetonate ($Co(acac)_2$, 97%, Sigma-Aldrich), tin(II) acetate ($Sn(oac)_2$, 95%, Fluka), tri-n-octylphosphine (TOP, 97%, Strem), oleylamine (OAm, 80-90%, TCI), borane tert-butylamine complex (TBAB, 97%, Sigma-Aldrich), oleic acid (OAc, Sigma-Aldrich), hydrazine monohydrate (N_2H_4, 64-65%, reagent grade, 98%, Sigma-Aldrich), Nafion (10 wt. %, perfluorinated ion-exchange resin, dispersion in water), methanol (anhydrous, 99.8%, Sigma-Aldrich), carbon black (CB, VULCAN XC72), potassium hydroxide (KOH, 85%, Sigma-Aldrich) and acetonitrile (CH_3CN, extra dry, Fisher) were used as received without any further treatment. Chloroform, hexane, acetone, and ethanol were of analytical grade and purchased from various sources. MilliQ water was obtained from a PURELAB flex from ELGA. An argon-filled glove-box was used for storing and handling sensitive chemicals.

Synthesis of colloidal $Ni_{3-x}Co_xSn_2$ NPs: All the syntheses were performed using standard airless techniques: a vacuum/dry argon gas Schlenk line was used for the synthesis. $Ni_{3-x}Co_xSn_2$ NPs were prepared following a similar protocol as the one we developed for the scale-up production of NiSn NPs.[58] In a typical synthesis of $Ni_{1.5}Co_{1.5}Sn_2$ NPs, 20 mL OAm, 0.3 mmol $Ni(acac)_2$, 0.3 mmol $Co(acac)_2$, 0.4 mmol $Sn(oac)_2$ and 1.0 mL OAc were loaded into a 50 mL three-necked flask and degassed under vacuum at 80 °C for 2 hours while being strongly stirred using a magnetic bar. Afterward, a gentle flow of argon was introduced, and then 5 mL of TOP was injected into the solution. Subsequently, the reaction flask was heated to 180 °C within 20 min, followed by quick injection of a solution containing 5 mmol TBAB in 5 mL degassed OAm. A visible color change, from deep pink to black was observed immediately. The reaction was maintained at this temperature for 1 hour before it was quenched using a water bath. The obtained NPs were collected by centrifuging and washing the solid product with acetone and chloroform 3 times. The as-prepared NPs were finally dispersed in chloroform and stored for further use. NPs were colloidally stable in chloroform for a couple of weeks. NPs with different nominal Ni/Co ratios, $Ni_{3-x}Co_xSn_2$ ($0 \le x \le 3$), were prepared following the same procedure (Scheme 1).

Ligand removal: As-synthesized $Ni_{3-x}Co_xSn_2$ NPs dispersed in chloroform were precipitated through addition of ethanol and centrifugation. Then, they were dispersed in a mixture containing 25 mL acetonitrile and 0.8 mL hydrazine hydrate and stirred for 4 hours. NPs were then collected by centrifugation and washed with acetonitrile 3 additional times. Finally, NPs were dried under vacuum.

Characterization: Powder x-ray diffraction (XRD) patterns were collected directly from the as-synthesized NPs on a Bruker AXS D8 Advance x-ray diffractometer with Ni-filtered (2 µm thickness) Cu K radiation (λ = 1.5106 Å) operating at 40 kV and 40 mA. 200 mesh carbon-coated transmission electron microscopy (TEM) grids from Ted-Pella were used as substrate. A drop of as-synthesized NPs dispersion was casted and dried on the grids before measurement. TEM analyses were carried out on a ZEISS LIBRA 120, operating at 120 kV. High-resolution TEM (HRTEM) and scanning TEM (STEM) studies were carried out using a field emission gun FEI Tecnai F20 microscope at 200 kV with a point-to-point resolution of 0.19 nm. High angle annular dark-field (HAADF) STEM was combined with electron energy loss spectroscopy (EELS) in the Tecnai microscope by using a GATAN QUANTUM filter. The Fourier transform infrared spectrometer (FTIR) data of the as-synthesized NPs before and after ligand removal were recorded on an Alpha Bruker FTIR spectrometer with a platinum attenuated total reflectance (ATR) single reflection module. Scanning electron microscopy (SEM) analyses were performed on a ZEISS Auriga SEM with an energy dispersive X-ray spectroscopy (EDS) detector at 20 kV. X-ray photoelectron spectroscopy (XPS) was done on a SPECS system equipped with an Al anode XR50 source operating at 150 mW and a Phoibos 150 MCD-9 detector. The pressure in the analysis chamber was kept below 10^{-7} Pa. The area analyzed was about 2 mm x 2 mm. The pass energy of the hemispherical analyzer was set at 25 eV and the energy step was maintained at 1.0 eV. Data processing was performed with the Casa XPS program (Casa Software Ltd., UK). Binding energies were shifted according to the reference C 1s peak that was located at 284.8 eV.

Preparation of Catalysts inks: In a typical preparation of a catalysts ink, 5 mg of purified NPs together with 5 mg of CB were added to 2 mL MilliQ water/ethanol solution (v/v = 1:1) containing 50 µL of a 10 wt% Nafion solution. Then the mixture was vigorously sonicated for 1 hour to obtain a homogeneous mixture. A glassy carbon (GC, 5 mm in diameter) electrode was polished using diamond paper and 0.05 µm alumina slurry, followed by water flush with MilliQ water. Subsequently, the electrode was ultra-sonicated in ethanol and MilliQ water separately for ~20 s before it was flushed with MilliQ water again and dried under argon flow at room temperature. Finally, 5 µL of the prepared ink was evenly loaded onto the GC electrode and was allowed to dry naturally in air at room temperature.

Electrochemical characterization: An electrochemical workstation (AutoLab, Metrohm) was employed for the electrochemical measurements in open air at room temperature. The conventional three-electrode system consisted of a counter electrode (Pt mesh), a working electrode and a reference electrode (*vs.* Hg/HgO). The Hg/HgO was placed in a salt bridge of 1.0 M KOH. All the measurements were performed in N_2-bubled 1.0 M KOH solution with and without addition of variable concentrations of methanol with magnetic bar stirring. All potential values presented in this paper were referred to the reference electrode, *vs.* Hg/HgO. Cyclic

voltammetry (CV) and chronoamperometry (CA) measurements were performed to investigate the activity and stability for MOR. The current densities were calculated taking into account the geometric surface area of the GC electrode (0.196 cm^{-2}) or the metal mass loading (~ 0.012 mg NPs). The CO poisoning experiments were conducted in 1.0 M KOH containing 1.0 M CH_3OH using CA at 0.6 V simply by introducing a gentle gas (10% CO + 90% He) flow into the solution.

DFT calculations: To figure out the change of activity of Ni_3Sn_2 surface with the introduction of Co atoms, the adsorption of CH_3OH on the Ni_3Sn_2 and $Ni_{2.5}Co_{0.5}Sn_2$ surfaces was investigated using the Vienna ab-initio simulation package (VASP) based on the density functional theory (DFT).[63–66] An eight-layers slab was constructed in our models. During the structural optimization calculations, the atoms in the two bottom layers were fixed in their bulk positions, and those in the other six layers were allowed to relax. The (001) and (110) surfaces of both Ni_3Sn_2 and $Ni_{2.5}Co_{0.5}Sn_2$ were employed in our DFT calculations. The adsorption energies of CH_3OH on the surfaces, ΔE_{ads}, was defined as follows

$$\Delta E_{ads} = E_{adsorbate/slab} - E_{slab} - E_{adsorbates}$$

where $E_{adsorbate/slab}$ is the total energy of CH_3OH on the surfaces, E_{slab} is the total energy of the isolate surfaces and $E_{adsorbate/slab}$ is the total energy of isolate CH_3OH molecule. The first two terms were calculated with the same parameters. The third term was calculated by setting the isolated adsorbate in a box of 20 Å × 20 Å × 20 Å. Thus, negative ΔE_{ads} indicates exothermic chemisorption and positive values indicate an endothermic process.

Results and discussion

Synthesis of $Ni_{3-x}Co_xSn_2$ colloidal NPs: $Ni_{3-x}Co_xSn_2$ ($0 \le x \le 3$) colloidal NPs were produced from the reduction of proper amounts of the different metal salts in the presence of TOP, OAm and OAc (see experimental section and Scheme 1 for details). Figures 1a and S1 display representative TEM micrographs of the quasi-spherical $Ni_{3-x}Co_xSn_2$ NPs produced. Table 1 displays the average diameter of NPs with different compositions. For the ternary compositions, a slight increase of size was obtained when increasing the amount of Co, from 4.2 ± 0.7 to 5.4 ± 0.8 nm. The size of the binary Co_3Sn_2 NPs was slightly larger, 7.5 ± 1.0 nm (Table 1).

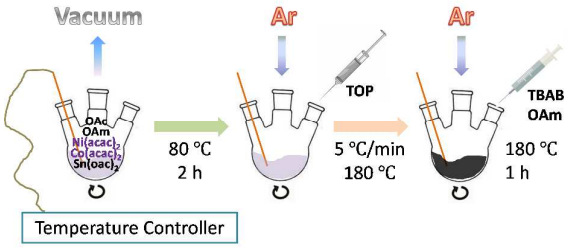

Scheme 1. Schematic drawing of the synthesis procedure produce $Ni_{3-x}Co_xSn_2$ NPs

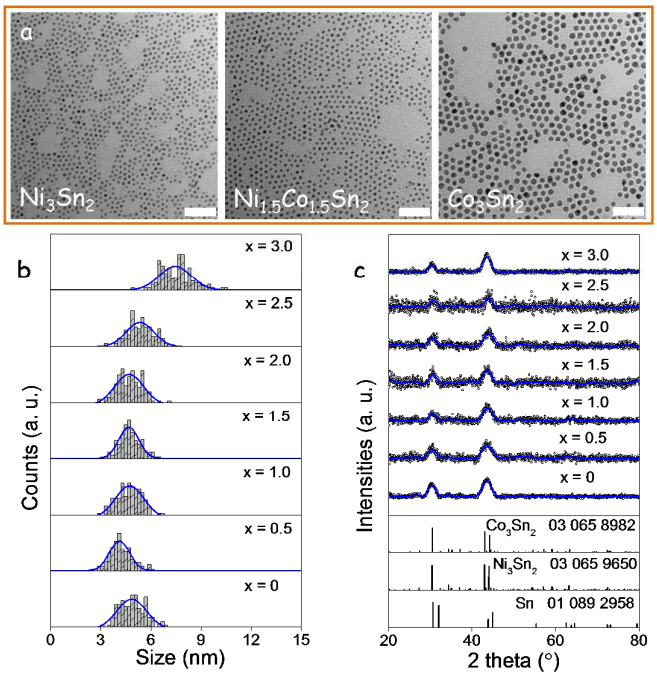

Figure 1. a) Representative TEM micrographs of $Ni_{3-x}Co_xSn_2$ NPs with different Co contents: x = 0, x = 1.5, x = 3.0. Scale bars: 50 nm. b) Size distribution histograms obtained from TEM images of $Ni_{3-x}Co_xSn_2$ ($0 \le x \le 3$) NPs. c) XRD patterns of $Ni_{3-x}Co_xSn_2$ ($0 \le x \le 3$) NPs.

Ni_3Sn_2 and Co_3Sn_2 share the same orthorhombic crystal phase (Pnam space group) and have very similar lattice parameters, owing to their virtually equal ionic radius (0.135 nm).[67,68] Thus, very similar XRD patterns were obtained for all compositions, although the XRD patterns of the ternary structures pointed at slightly more defective crystals (Figure 1c).

EDX analyses showed all compositions to be Sn-rich (Figure S2 and Table 1), i.e. (Ni+Co)/Sn < 1.5. The Ni/Co ratio obtained by EDX analyses matched relatively well the nominal composition, which was not surprising taking into account the similitude of the two elements, with similar standard reduction potentials, Ni^{2+} (-0.25 V) and Co^{2+} (-0.28 V). [68]

Table 1. Average NPs size (TEM) and Ni:Co:Sn composition of $Ni_{3-x}Co_xSn_2$ NPs.

x	Average Size	EDX			
$Ni_{3-x}Co_xSn_2$	(nm)	Ni	Co	Sn*	(Ni+Co)/Sn
0.0	4.9 ± 0.8	2.5	0.0	2.0	1.25
0.5	4.2 ± 0.7	1.8	0.3	2.0	1.05
1.0	4.7 ± 0.7	1.4	0.7	2.0	1.05
1.5	4.7 ± 0.7	1.3	1.3	2.0	1.30
2.0	4.7 ± 0.7	0.8	1.4	2.0	1.10
2.5	5.4 ± 0.8	0.4	1.9	2.0	1.15
3.0	7.5 ± 1.0	0.0	2.1	2.0	1.05

*The amount of Sn was fixed to 2.0 to calculate the Ni and Co composition.

Figure 2 shows HAADF-STEM, EELS compositional mappings and HRTEM micrographs of $Ni_{2.5}Co_{0.5}Sn_2$ NPs (see Figure S3 for additional compositions). All NPs within each sample contained the three elements in similar ratios. Within each NP, the three elements were found to be homogeneous distributed. HRTEM micrographs revealed NPs to have a crystal structure compatible with that of Ni_3Sn_2 orthorhombic phase (space group = Pnma) with a = 7.1100 Å, b = 5.2100 Å and c = 8.2300 Å.

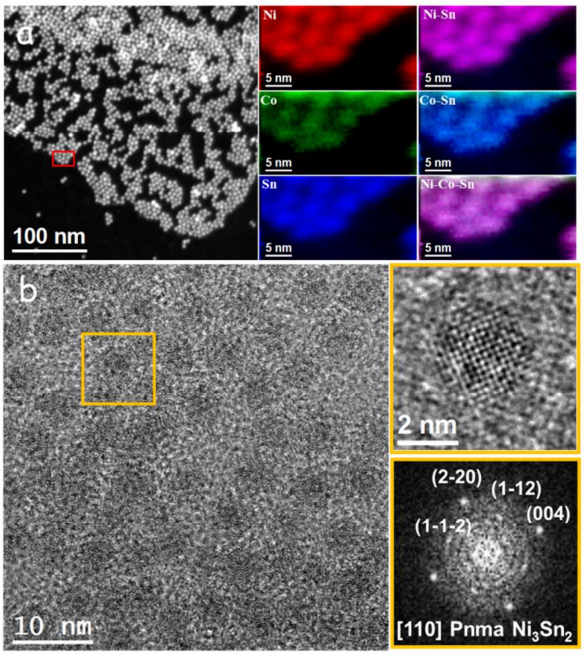

Figure 2. a) STEM micrograph and EELS chemical composition maps for $Ni_{2.5}Co_{0.5}Sn_2$ NPs. Mappings correspond to the individual Ni $L_{2,3}$-edges at 855 eV (red), Co $L_{2,3}$-edges at 779 eV (green) and Sn M-edge at 485 eV (blue) as well as composites of Ni-Sn, Co-Sn and Ni-Co-Sn. b) HRTEM micrograph, detail of the orange squared region and its corresponding power spectrum. Lattice fringe distances were measured to be 0.211 nm, 0.205 nm, 0.306 nm and 0.302 nm, at 89.14º, 44.38º and 50.22º which could be interpreted as the orthorhombic Ni_3Sn_2 phase visualized along its [110] zone axis.

XPS analyses of the $Ni_{1.5}Co_{1.5}Sn_2$ sample showed all elements to be present in two oxidation states: a minoritary metallic state and a majoritarian oxidized phase (Figure S4). This result pointed at a partial surface oxidation of the NPs occurring due to their air exposure during purification, ligand removal and handling process.[58,69,70] Additionally, XPS analysis showed the $Ni_{1.5}Co_{1.5}Sn_2$ NPs to be slightly Sn rich, with (Ni + Co)/Sn = 0.91.

The presence of organic ligands at the surface of NPs strongly limits their electronic interaction and their ability to interact with the media.[37] Therefore, the use of NPs for applications where charge transfer or transport is involved requires the removal of the organic ligands used in the synthesis. Organic ligands were removed from the surface of $Ni_{3-x}Co_xSn_2$ NPs using a solution containing a 1 M hydrazine hydrate in acetonitrile.[71,72] After successive cleaning with acetonitrile, the disappearance of peaks at 2890 and 2822 cm^{-1} in the FTIR spectra, corresponding to C-H stretching modes, proved the effectiveness of the ligand removal (Figure S5).

Electrochemical characterization: In our previous report, we showed electrodes based on Sn NPs to show no oxidation and reduction peaks in the voltage range 0-0.6 V *vs*. Hg/HgO and a very limited performance toward MOR and OER in alkaline medium.[58] On the other hand, in alkaline medium, Co is found in an oxidized form.[73–75] During the forward scan, at 0.15 V *vs*. Hg/HgO, cobalt is further oxidized probably to CoOOH and at ca. 0.55 V vs. Hg/HgO, CoOOH is possibly oxidized to CoO_2.[54,57,75,76] These phases are reduced during the reverse scan.

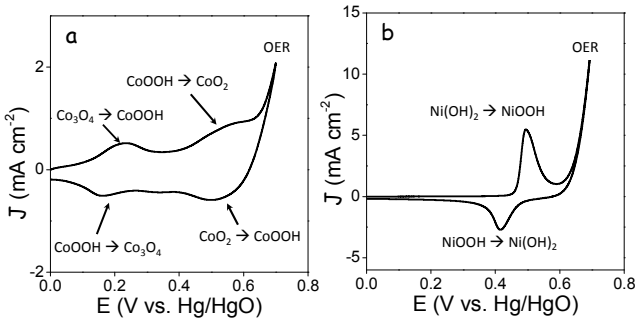

Figure 3. a) CV of Co_3Sn_2 electrodes in 1 M KOH solution at a scan rate of 50 mV s^{-1}. Tentative reduction and oxidation products are displayed. b) CV of Ni_3Sn_2 electrodes in 1 M KOH solution at a scan rate of 50 mV s^{-1}.

Figure 3a displays a CV of Co_3Sn_2 NPs in 1 M KOH at a scan rate of 50 mV s^{-1}. Co_3Sn_2 NPs show a low activity toward OER and small oxidation and reduction peaks during the positive and negative scans in the potential range 0-1.0 V *vs.* Hg/HgO, which correspond to the successive oxidation and reduction between cobalt oxide, hydroxide and/or oxyhydroxide phases.

In alkaline medium, Ni is generally found in the form of $Ni(OH)_2$, which is oxidized to NiOOH at 0.45 V vs. Hg/HgO.[58,77–80] The formation of the nickel oxyhydroxide is considered to be a key step in the electro-catalytic OER, which activates at E~0.65 V *vs*. Hg/HgO.[41,56] Figure 3b displays a CV of the electrode based on Ni_3Sn_2 NPs where the anodic peak corresponding to the oxidation of $Ni(OH)_2$ to NiOOH at 0.45 V vs. Hg/HgO is observed. In the reverse scan, a cathodic peak corresponding to the reduction of NiOOH to $Ni(OH)_2$ is clearly observed.

Figure 4a shows representative CVs of the $Ni_{3-x}Co_xSn_2$ electrodes in 1 M KOH solution at 50 mV s^{-1}. Compared with Ni_3Sn_2, when increasing the content of Co ($0 < x < 1.5$) the anodic peak broadened and shifted to lower potentials, denoting a clear influence of Co on the Ni_3Sn_2 alloy surface properties. At higher amounts of Co ($x \geq 1.5$), a double peak was clearly observed, pointing at the occurrence of two differentiated oxidation reactions. Similar trends were observed for the cathodic peak. Simultaneously, the peak current densities increased when adding small amounts of Co, but decreased at higher Co loading (Table 2).

Figures 4b and S6a-e present the CV of $Ni_{3-x}Co_xSn_2$ in 1.0 M KOH solution obtained at different scan rates, between 10 and 100 mV s^{-1}. When increasing the scan rate, current densities increased, the position of the anodic peak shifted to higher potentials, and the position of the cathodic peak shifted to lower potentials. The peak shift was attributed to a limitation of the reaction kinetics, which we further analyzed.[81] In the samples containing larger amounts of

Co and presenting two redox peaks, we assumed the peak at higher potential values, related to a $Ni(OH)_2$ oxidation to NiOOH to be the relevant in the MOR. Therefore, we just considered the peak at the highest potential values in the following calculations.

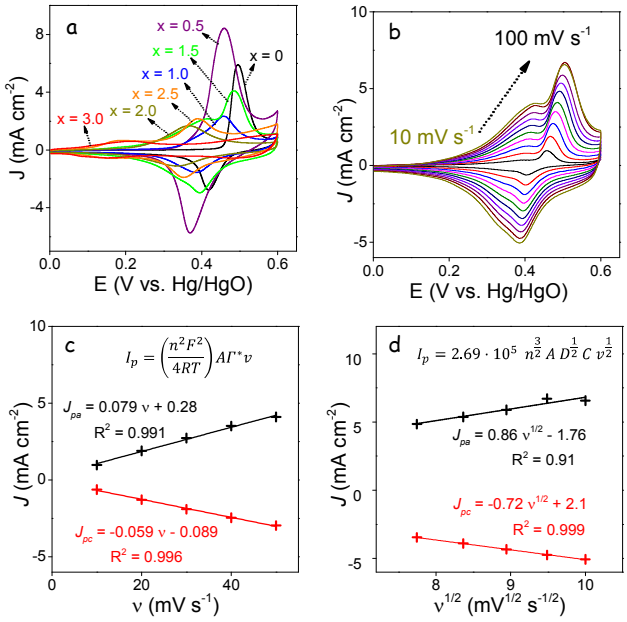

Figure 4. a) CVs of $Ni_{3-x}Co_xSn_2$ NP-based electrodes in 1.0 M KOH solution at a scan rate of 50 mV s^{-1}. b) CVs of electrodes based on $Ni_{1.5}Co_{1.5}Sn_2$ (x = 1.5) NPs in 1.0 M KOH solution at increasingly higher potential sweep rates: 10, 20, 30, 40, 50, 60, 70, 80, 90, 100 mV·s^{-1}. c) Linear fitting of the anodic and cathodic peak current densities with the scan rate in the low scan rate range (10-50 mV s^{-1}) for the $Ni_{1.5}Co_{1.5}Sn_2$ NP-based electrode. d) Linear fitting of the anodic and cathodic peak current densities with the square roots of the scan rate in the higher scan rate range (60-100 mV s^{-1}) for the $Ni_{1.5}Co_{1.5}Sn_2$ NP-based electrode.

The peak current (I_P) was proportional to the sweep rate (v) in the range 10-50 mV s^{-1}. From the slope of I_P vs. v (Figures 5c and S7), the surface coverage of redox species (Γ^*) in the $Ni_{3-x}Co_xSn_2$ NPs was estimated[58,82]:

$$I_p = \left(\frac{n^2F^2}{4RT}\right)A\Gamma^* v$$

Where n, F, R, T and A are the number of transferred electrons (assumed to be 1), the Faraday constant (96845 C mol^{-1}), the gas constant (8.314 J K^{-1} mol^{-1}), temperature and the geometric surface area of the GC electrodes (0.196 cm^2), respectively.

Averaging results obtained from the forward and reverse scans, the surface coverage of redox species of Ni_3Sn_2 NPs-based electrodes was calculated to be 8.6 × 10^{-8} mol cm^{-2}. When introducing a small amount of Co, $Ni_{2.5}Co_{0.5}Sn_2$, this surface coverage increased to 1.4 × 10^{-7} mol cm^{-2}. Higher amounts of Co decreased this coverage to values below that of Ni_3Sn_2.

In the high scan rate range, 60-100 mV s^{-1}, the peak current increased linearly with the square root of the voltage scan rate, pointing toward a diffusion-limited redox reaction[58,82]:

$$I_p = 2.69 \times 10^5 n^{3/2} A D^{1/2} C v^{1/2}$$

where D is the diffusion coefficient of the reaction limiting specie and C is the initial concentration of redox species. Qualitatively, we observed the slope of I_P vs. $v^{1/2}$ obtained from Ni_3Sn_2 NP-based electrodes to increase when adding small amounts of Co. This observation pointed out at a faster diffusion of the redox limiting specie with the incorporation of Co. For Ni-based electrodes, the proton diffusion is generally accepted to be the rate limiting step that controls the oxidation reaction $Ni(OH)_2 \leftrightarrow NiOOH$.[58,83] Therefore, using the above equation and taking into account a proton density of 0.043 mol cm^{-3} for all the electrodes, the proton diffusion coefficient of the different materials was estimated.[58] The proton diffusion coefficient of Ni_3Sn_2 NP-based electrodes was 8.4 × 10^{-9} cm^2 s^{-1}. As qualitatively noted before, the diffusivity increased when introducing a small amount of Co within the structure: 1.3 × 10^{-8} cm^2 s^{-1} for $Ni_{2.5}Co_{0.5}Sn_2$, but decreased at higher Co concentrations: 2.9 × 10^{-9} cm^2 s^{-1} for Ni_2CoSn_2, and 4.6 × 10^{-9} cm^2 s^{-1} for $Ni_{1.5}Co_{1.5}Sn_2$.

Table 2. Summary of the electrocatalytic performance of $Ni_{3-x}Co_xSn_2$ NP-based electrodes

x	E_{pa} V vs Hg/HgO	J_{pa} mA cm^{-2}	E_{pc} V vs Hg/HgO	J_{pa} mA cm^{-2}	ΔE V	Γ^* mol cm^{-2} (×10^{-8})	D cm^2 s^{-1} (×10^{-9})	E_η V *10 mA cm^{-2}*	J *mA cm^{-2} @0.6 V*	*ΔJ @0.6 V*
0	0.496	5.934	0.417	-2.765	0.079	8.6	8.4	0.525	34.4	-15.2%
0.5	0.461	8.436	0.369	-5.756	0.092	14.2	12.8	0.452	65.5	-23.5%
1.0	0.457	2.351	0.383	-1.564	0.074	4.1	2.9	0.479	51.8	-40.8%
1.5	0.486	3.921	0.393	-2.970	0.093	7.3	4.6	0.464	53.8	-31.7%
2.0	0.364	1.682	0.330	-1.125	0.034	3.1	2.2	0.483	39.4	-81.4%
2.5	0.391	2.187	0.356	-1.903	0.035	4.7	4.2	0.481	34.4	-64.2%
3.0	0.207	0.579	0.172	-0.541	0.035	-	-	-	-	-

Note: In samples showing two anodic/cathodic peaks, J_{pa}, E_{pa}, J_{pc}, E_{pc} and ΔE were measured from the highest voltage peak. CVs were carried out in 1.0 M KOH solution at a scan rate of 50 mV s^{-1}. E_η, J, ΔJ were calculated from the CVs in 1.0 M KOH solution containing 2.0 M methanol at a scan rate of 50 mV s^{-1}.

Electrocatalytic activity toward MOR: Figure S6 compares the cyclic voltammograms in 1.0 M KOH solution of electrodes based on Co_3Sn_2 and Ni_3Sn_2 NPs in absence and presence of a low concentration of methanol (0.5 M). Co_3Sn_2 showed much lower activities than the Ni_3Sn_2 catalyst toward both OER and MOR. The OER onset was found at ca. 0.65 V vs. Hg/HgO for both samples. While no significant MOR activity was appreciated in the Co_3Sn_2 electrode, MOR was activated at ca 0.45 V vs. Hg/HgO in Ni_3Sn_2-based electrodes. This voltage coincided with the formation of NiOOH. Indeed, it is generally accepted that in Ni-based catalysts, MOR is activated by the formation of the NiOOH, which is believed to directly participate in the reaction.[41,46,58]

$$Ni(OH)_2 + OH^- \Rightarrow NiOOH + H_2O + e^-$$

$$NiOOH + CH_3OH \Rightarrow Ni(OH)_2 + products$$

To avoid the OER in the test of the MOR over $Ni_{3-x}Co_xSn_2$ NP-based electrodes, the potential range scanned was limited to 0-0.6 V *vs.* Hg/HgO.

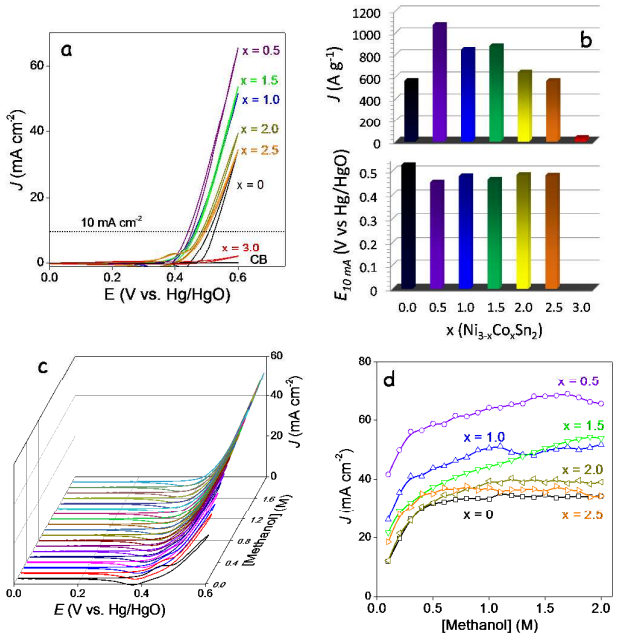

Figure 5. a) CVs of $Ni_{3-x}Co_xSn_2$ ($0 \le x \le 3$) and CB electrode in 1.0 M KOH containing 2.0 M methanol at a scan rate of 50 mV s^{-1}. b) Mass current density and applied potential required to reach 10 mA cm^{-2} in $Ni_{3-x}Co_xSn_2$ ($0 \le x \le 3$) electrodes at 0.6 V in 1.0 M KOH with 2.0 M methanol. c) CVs of a $Ni_{1.5}Co_{1.5}Sn_2$ electrode in 1.0 M KOH solution with different methanol concentrations from 0.1 M to 2.0 M at a scan rate of 50 mV s^{-1}. d) Comparison of the current density at 0.6 V of $Ni_{3-x}Co_xSn_2$ ($0 \le x \le 2.5$) electrodes as a function of methanol concentrations from 0.1 M to 2.0 M.

Figure 5a shows CVs of a bare carbon black electrode and $Ni_{3-x}Co_xSn_2$ NP-based electrodes in 1.0 M KOH solution with 2 M methanol at a scan rate of 50 mV s^{-1}. Co_3Sn_2 presented very limited current densities toward MOR, similar to the carbon black electrode. However, surprisingly, all $Ni_{3-x}Co_xSn_2$ NP-based electrodes showed higher activity than the Ni_3Sn_2 NP-based electrode, including a lower onset potential and higher mass current densities. The onset potential (@ 10 mA cm^{-2}) was reduced from 0.53 V for Ni_3Sn_2 to 0.45 V for $Ni_{2.5}Co_{0.5}Sn_2$ and 0.46-0.48 V for the other Co-containing NP-based electrodes (Figure 5). Similarly, the mass current density increased with the incorporation of Co to the Ni_3Sn_2 alloy, from 562.6 A g^{-1} for Ni_3Sn_2 to 1070 A g^{-1} for the $Ni_{2.5}Co_{0.5}Sn_2$ electrode (Figure 5b). At higher Co/Ni ratios, the mass current density decreased with the Co content, but was kept above that of Ni_3Sn_2. In Table S1 a comparison of the performance toward MOR of the $Ni_{3-x}Co_xSn_2$ NP-based electrodes with other Ni-based electrodes and a commercial Pt/C composite is presented. The comparison demonstrated that $Ni_{3-x}Co_xSn_2$ NP-based electrodes with a preliminary optimized composition, $Ni_{2.5}Co_{0.5}Sn_2$, outperformed most previously developed catalysts.

Figures 5c, S8 and S9 show the CVs of $Ni_{3-x}Co_xSn_2$ NP-based electrodes in 1.0 M KOH solution with 0.1-2.0 M methanol at a scan rate of 50 mV s^{-1}. Figures 5d and S7 present the current density at 0.6 V in 1.0 M KOH as a function of the methanol concentrations, from 0.1 to 2.0 M. For all electrodes, an initial rapid rise of the current density with the methanol concentration was observed. For Ni_3Sn_2, $Ni_{1.0}Co_{2.0}Sn_2$ and $Ni_{0.5}Co_{2.5}Sn_2$ electrodes, the current density stabilized at concentrations higher than 0.5 M methanol. However, the electrodes with a low Co loading still showed a slight increase of the current density above this concentration, which should be associated to a lower poisoning of the active sites by methanol adsorption in $Ni_{3-x}Co_xSn_2$ ($x \le 1.5$) NPs compared with Ni_3Sn_2 NPs (Figures 5c, S8 and S9). In particular, at 0.6 V *vs.* Hg/HgO, the $Ni_{2.5}Co_{0.5}Sn_2$ electrode displayed a current density of 41 mA cm^{-2} at 0.1 M, 59 mA cm^{-2} at 0.5 M and 65 mA cm^{-2} at 2.0 M. On the other hand, the Ni_3Sn_2 electrode was characterized by a current density of 12 mA cm^{-2} at 0.1 M, 32 mA cm^{-2} at 0.5 M and 34 mA cm^{-2} at 2.0 M at 0.6 V.

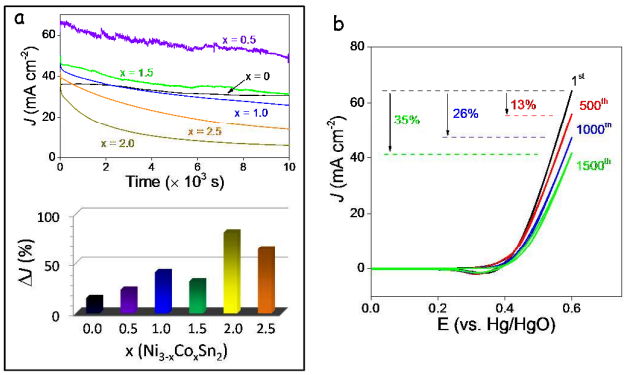

Figure 6. a) CA response of $Ni_{3-x}Co_xSn_2$ electrodes in 1.0 M KOH and 2.0 M methanol at 0.6 V for 10000 s. Current density change, $\Delta J = (J_1-J_2)/J_1$, during the 10000s tested, where J_1 and J_2 are the current densities measured at the 50th and 10000th s respectively. b) CVs of the $Ni_{2.5}Co_{0.5}Sn_2$ electrode in 1.0 M KOH electrolyte with 2.0 M methanol at a scan rate of 100 mV s^{-1} at cycles 1st, 500th, 1000th and 1500th.

The long-term stability of $Ni_{3-x}Co_xSn_2$ NP-based electrodes was evaluated by CA measurements in 1.0 M KOH solution containing 2.0 M methanol at 0.60 V for 10000 s (Figure 6a). While an

improved performance toward high methanol concentrations was obtained with the addition of small amounts of Co, the electrode stability decreased when adding increasingly higher amounts of Co, being the Ni_3Sn_2 electrode the most stable, followed by the $Ni_{2.5}Co_{0.5}Sn_2$. The stability of the $Ni_{2.5}Co_{0.5}Sn_2$ electrode was also evaluated in the same concentration of methanol with continuous CV scanning with 100 mV s^{-1}. As shown in Figure 6b, the electrode lost 12.9% (500 circles), 21.5% (1000 circles) and 35.1% (1500 circles) of the current density of the 1st CV at 0.6 V. This performance decay could have its origin on: i) the progressive poisoning of the active sites by the reaction intermediates/products, ii) a restructuration of the alloy NPs or change of the NP electronic or chemical properties during the reaction, potentially related to the presence of cobalt.

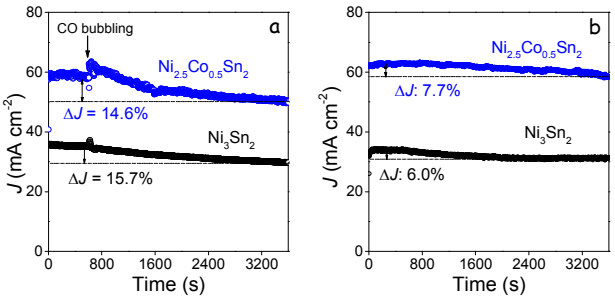

Figure 7. CA of Ni_3Sn_2 NPs and $Ni_{2.5}Co_{0.5}Sn_2$ NPs in 1.0 M KOH and 1.0 M methanol at 0.6 V: a) In the presence of a gentle CO flow (10% in He) added at t = 600 s. b) Without additional CO incorporation to the solution. $\Delta J = (J_1-J_2)/J_1$, where J_1 and J_2 is the current density measured at 600th and 3600th s respectively.

CO is generally considered as the most common intermediate/product degrading the catalyst performance over time through the blocking of its active sites.[34,40,42,55,57] Additional CA measurements were performed on the electrodes based on Ni_3Sn_2 NPs and $Ni_{2.5}Co_{0.5}Sn_2$ NPs in 1.0 M KOH and 1.0 M methanol at 0.6 V (Figure 7). At a certain time (t = 600 s), a gentle flow of CO was bubbled into the solution to determine its effect on the current density. With the presence of additional CO, both electrodes suffered a similar loss in the current density: 14.9% for $Ni_{2.5}Co_{0.5}Sn_2$ and 15.6% for Ni_3Sn_2. The same experiment in the absence of CO resulted in a significantly larger decrease of current density for the $Ni_{2.5}Co_{0.5}Sn_2$ electrode: 7.7% for $Ni_{2.5}Co_{0.5}Sn_2$ and 6.0% for Ni_3Sn_2. This result demonstrates the Co-containing electrode not to be specially sensitive to CO poisoning when compared with the Ni_3Sn_2-based one.

DFT calculations: Complementary to the experimental work, to gain insight of the electronic effect that the Co incorporation had on the Ni_3Sn_2 alloy, DFT calculations of the surface of the metallic alloys were performed (see details in experimental section and Figures S10-13). DFT calculations showed that the adsorption energies of methanol (E_{ads}) on Ni sites at Ni_3Sn_2 (001) and (110) facets were -0.57 eV and -0.49 eV. These values slightly increased for Ni sites at $Ni_{2.5}Co_{0.5}Sn_2$ surfaces: -0.59 eV and -0.74 eV for $Ni_{2.5}Co_{0.5}Sn_2$ (001) and (110), respectively. The adsorption energies of methanol on Co sites at $Ni_{2.5}Co_{0.5}Sn_2$ (001) and (110) surfaces were -0.63 eV and -0.52 eV, respectively. The higher absolute values of E_{ads} on Ni than Co in $Ni_{2.5}Co_{0.5}Sn_2$ surfaces pointed out at the preferential absorption of methanol molecules on the former. The higher E_{ads} obtained from the ternary alloy should imply a higher methanol poisoning not observed in the measurements of the current density as a function of the methanol concentration. On the other hand, the adsorption energies of CO on Ni sites at $Ni_{2.5}Co_{0.5}Sn_{2.0}$ (001) and (110) surfaces, -2.46 eV and -2.16 eV, were also higher than on Ni_3Sn_2 (001) and (110), -2.07 eV and -1.98 eV, which could result in a higher CO poisoning that was neither reflected in our experimental results. Further comprehensive DFT calculations including all the reaction steps and the proper alloy composition under reaction conditions would be required to evaluate the exact MOR mechanism.

Conclusions

In summary, a series of $Ni_{3-x}Co_xSn_2$ ($0 \le x \le 3$) quasi-spherical NPs with narrow size distribution were synthesized by a solution-based one-pot method. Detailed catalytic investigation of methanol oxidation showed that the introduction of small amounts of Co in the structure improved the electrocatalytic performance. A preliminary optimized catalyst composition, $Ni_{2.5}Co_{0.5}Sn_2$, showed 65.5 mA cm^{-2} and a mass current density of 1050 mA mg^{-1} at 0.6 V *vs.* Hg/HgO for MOR in 1.0 M KOH containing 1.0 M methanol. While the introduction of Co slightly decreased durability, $Ni_{2.5}Co_{0.5}Sn_2$ NP-based electrodes demonstrated a significant stability during continuous cycling and increased activity at high methanol concentrations. Its excellent activity and stability towards MOR suggested an attractive anode material for DMFCs.

Conflicts of interest

There are no conflicts to declare.

Acknowledgements

This work was supported by the European Regional Development Funds and by the Spanish Ministerio de Economía y Competitividad through the project SEHTOP (ENE2016-77798-C4-3-R) and VALPEC (ENE2017-85087-C3). J. Li and T. Zhang thank the China Scholarship Council (CSC) for scholarship support. T. Zhang and J. Arbiol acknowledge funding from Generalitat de Catalunya 2017 SGR 327. ICN2 acknowledges support from the Severo Ochoa Programme (MINECO, Grant no. SEV-2013-0295). IREC and ICN2 are funded by the CERCA Programme / Generalitat de Catalunya. Part of the present work has been performed in the framework of Universitat Autònoma de Barcelona Materials Science PhD program. J. Llorca is a Serra Húnter Fellow and is grateful to ICREA Academia program and to MINECO/FEDER grant ENE2015-63969-R and GC 2017 SGR 128.

Author Contributions

The manuscript was prepared through the contribution of all authors. A. Cabot and Z. Luo conceived and guided the project,

and supervised the work. J. Li designed the experiments, produced the nanoparticles, conducted XRD, TEM, SEM-EDS and FT-IR characterization, electrochemical measurements, and wrote the first draft of the manuscript. F. He carried out the DFT calculations. Y. Zuo, J. Liu, X. Yu and R. Du significantly contributed to the results discussion. T. Zhang, M. F. Infante-Carrió, P. Tang and J. Arbiol performed structural and compositional NCs characterization by means of HRTEM and EELS, and discussed the results. J. Llorca measured and discussed XPS data. The manuscript was corrected and improved by all authors.

Notes and references

1 X. Zhou, J. Qiao, L. Yang and J. Zhang, *Adv. Energy Mater.*, 2014, **4**, 1301523.

2 N. Demirdöven and J. Deutch, *Science*, 2004, **305**, 974–6.

3 X. Zhao, M. Yin, L. Ma, L. Liang, C. Liu, J. Liao, T. Lu and W. Xing, *Energy Environ. Sci.*, 2011, **4**, 2736.

4 T. Schultz, S. Zhou and K. Sundmacher, *Chem. Eng. Technol.*, 2001, **24**, 1223–1233.

5 Y. Feng, H. Liu and J. Yang, *Sci. Adv.*, 2017, **3**, e1700580.

6 J. N. Tiwari, R. N. Tiwari, G. Singh and K. S. Kim, *Nano Energy*, 2013, **2**, 553–578.

7 H. Huang and X. Wang, *J. Mater. Chem. A*, 2014, **2**, 6266–6291.

8 S. Wasmus and A. Küver, *J. Electroanal. Chem.*, 1999, **461**, 14–31.

9 G. A. Tritsaris and J. Rossmeisl, *J. Phys. Chem. C*, 2012, **116**, 11980–11986.

10 N. Kakati, J. Maiti, S. H. Lee, S. H. Jee, B. Viswanathan and Y. S. Yoon, *Chem. Rev.*, 2014, **114**, 12397–12429.

11 S. P. S. Badwal, S. Giddey, A. Kulkarni, J. Goel and S. Basu, *Appl. Energy*, 2015, **145**, 80–103.

12 S. S. Munjewar, S. B. Thombre and R. K. Mallick, *Ionics (Kiel).*, 2017, **23**, 1–18.

13 S. K. Kamarudin, F. Achmad and W. R. W. Daud, *Int. J. Hydrogen Energy*, 2009, **34**, 6902–6916.

14 S. S. Munjewar, S. B. Thombre and R. K. Mallick, *Renew. Sustain. Energy Rev.*, 2017, **67**, 1087–1104.

15 P. Kumar, K. Dutta, S. Das and P. P. Kundu, *Int. J. Energy Res.*, 2014, **38**, 1367–1390.

16 L. R. Merte, M. Ahmadi, F. Behafarid, L. K. Ono, E. Lira, J. Matos, L. Li, J. C. Yang and B. Roldan Cuenya, *ACS Catal.*, 2013, **3**, 1460–1468.

17 K. Sasaki, H. Naohara, Y. Choi, Y. Cai, W.-F. Chen, P. Liu and R. R. Adzic, *Nat. Commun.*, 2012, **3**, 1115.

18 Z. Daşdelen, Y. Yıldız, S. Eriş and F. Şen, *Appl. Catal. B Environ.*, 2017, **219**, 511–516.

19 C. Cui, L. Gan, M. Heggen, S. Rudi and P. Strasser, *Nat. Mater.*, 2013, **12**, 765–771.

20 S. Wu, J. Liu, D. Liang, H. Sun, Y. Ye, Z. Tian and C. Liang, *Nano Energy*, 2016, **26**, 699–707.

21 G. Long, X. Li, K. Wan, Z. Liang, J. Piao and P. Tsiakaras, *Appl. Catal. B Environ.*, 2017, **203**, 541–548.

22 J. Chen, Q. Niu, G. Chen, J. Nie and G. Ma, *J. Phys. Chem. C*, 2017, **121**, 1463–1471.

23 Q. Jiang, L. Jiang, H. Hou, J. Qi, S. Wang and G. Sun, *J. Phys. Chem. C*, 2010, **114**, 19714–19722.

24 K. W. Park, J. H. Choi, B. K. Kwon, S. A. Lee, Y. E. Sung, H. Y. Ha, S. A. Hong, H. Kim and A. Wieckowski, *J. Phys. Chem. B*, 2002, **106**, 1869–1877.

25 L. Li, Y. Wu, J. Lu, C. Nan and Y. Li, *Chem. Commun.*, 2013, **49**, 7486.

26 K.-W. Park, J.-H. Choi and Y.-E. Sung, *J. Phys. Chem. B*, 2003, **107**, 5851–5856.

27 S. Wang, G. Yang and S. Yang, *J. Phys. Chem. C*, 2015, **119**, 27938–27945.

28 L.-X. Ding, G.-R. Li, Z.-L. Wang, Z.-Q. Liu, H. Liu and Y.-X. Tong, *Chem. - A Eur. J.*, 2012, **18**, 8386–8391.

29 S. Papadimitriou, S. Armyanov, E. Valova, A. Hubin, O. Steenhaut, E. Pavlidou, G. Kokkinidis and S. Sotiropoulos, *J. Phys. Chem. C*, 2010, **114**, 5217–5223.

30 S. Chen, P. J. Ferreira, W. Sheng, N. Yabuuchi, L. F. Allard and Y. Shao-Horn, *J. Am. Chem. Soc.*, 2008, **130**, 13818–13819.

31 Y. Ma, L. Yin, T. Yang, Q. Huang, M. He, H. Zhao, D. Zhang, M. Wang and Z. Tong, *ACS Appl. Mater. Interfaces*, 2017, **9**, 36164–36172.

32 Y. Liao, G. Yu, Y. Zhang, T. Guo, F. Chang and C.-J. Zhong, *J. Phys. Chem. C*, 2016, **120**, 10476–10484.

33 H.-J. Qiu, X. Shen, J. Q. Wang, A. Hirata, T. Fujita, Y. Wang and M. W. Chen, *ACS Catal.*, 2015, **5**, 3779–3785.

34 G. You, J. Jiang, M. Li, L. Li, D. Tang, J. Zhang, X. C. Zeng and R. He, *ACS Catal.*, 2018, **8**, 132–143.

35 Y. Liu, M. Chi, V. Mazumder, K. L. More, S. Soled, J. D. Henao and S. Sun, *Chem. Mater.*, 2011, **23**, 4199–4203.

36 Y. Liu, D. Li, V. R. Stamenkovic, S. Soled, J. D. Henao and S. Sun, *ACS Catal.*, 2011, **1**, 1719–1723.

37 Z. Luo, J. Lu, C. Flox, R. Nafria, A. Genç, J. Arbiol, J. Llorca, M. Ibáñez, J. R. Morante and A. Cabot, *J. Mater. Chem. A*, 2016, **4**, 16706–16713.

38 F. Han, X. Wang, J. Lian and Y. Wang, *Carbon N. Y.*, 2012, **50**, 5498–5504.

39 X. Wang, J. Lian and Y. Wang, *Int. J. Hydrogen Energy*, 2014, **39**, 14288–14295.

40 D. Lim, D. Choi, W. Lee and H. Lee, *Appl. Catal.*, 2009, **89**, 484–493.

41 D. Wu, W. Zhang and D. Cheng, *ACS Appl. Mater. Interfaces*, 2017, **9**, 19843–19851.

42 W. Huang, H. Wang, J. Zhou, J. Wang, P. N. Duchesne, D. Muir, P. Zhang, N. Han, F. Zhao, M. Zeng, J. Zhong, C. Jin, Y. Li, S.-T. Lee and H. Dai, *Nat. Commun.*, 2015, **6**, 10035.

43 A. Serov and C. Kwak, *Appl. Catal. B Environ.*, 2009, **90**, 313–320.

44 I. Danaee, M. Jafarian, F. Forouzandeh, F. Gobal and M. G. Mahjani, *Int. J. Hydrogen Energy*, 2009, **34**, 859–869.

45 I. Danaee, M. Jafarian, F. Forouzandeh, F. Gobal and M. G. Mahjani, *Int. J. Hydrogen Energy*, 2008, **33**, 4367–4376.

46 X. Cui, P. Xiao, J. Wang, M. Zhou, W. Guo, Y. Yang, Y. He, Z. Wang, Y. Yang, Y. Zhang and Z. Lin, *Angew. Chemie Int. Ed.*, 2017, **56**, 4488–4493.

47 I. Danaee, M. Jafarian, A. Mirzapoor, F. Gobal and M. G. Mahjani, *Electrochim. Acta*, 2010, **55**, 2093–2100.

48 S. L. Candelaria, N. M. Bedford, T. J. Woehl, N. S. Rentz, A. R. Showalter, S. Pylypenko, B. A. Bunker, S. Lee, B. Reinhart, Y. Ren, S. P. Ertem, E. B. Coughlin, N. A. Sather, J. L. Horan, A. M. Herring and L. F. Greenlee, *ACS Catal.*, 2017, **7**, 365–379.

49 Y. Vlamidis, S. Fiorilli, M. Giorgetti, I. Gualandi, E. Scavetta and D. Tonelli, *RSC Adv.*, 2016, **6**, 110976–110985.

50 A. Roy, H. S. Jadhav, G. M. Thorat and J. G. Seo, *New J. Chem.*, 2017, **41**, 9546–9553.

51 S. Samanta, K. Bhunia, D. Pradhan, B. Satpati and R. Srivastava, *ACS Sustain. Chem. Eng.*, 2018, **6**, 2023–2036.

52 N. A. M. Barakat, M. Motlak, B.-S. Kim, A. G. El-Deen, S. S. Al-Deyab and A. M. Hamza, *J. Mol. Catal. A Chem.*, 2014, **394**, 177–187.

53 T. Rostami, M. Jafarian, S. Miandari, M. G. Mahjani and F. Gobal, *Chinese J. Catal.*, 2015, **36**, 1867–1874.

54 P. Manivasakan, P. Ramasamy and J. Kim, *Nanoscale*, 2014, **6**, 9665–9672.

55 E. Umeshbabu and G. Ranga Rao, *Electrochim. Acta*, 2016, **213**, 717–729.

56 X. Cui, Y. Yang, Y. Li, F. Liu, H. Peng, Y. Zhang and P. Xiao, *J. Electrochem. Soc.*, 2015, **162**, F1415–F1424.

57 X. Cui, W. Guo, M. Zhou, Y. Yang, Y. Li, P. Xiao, Y. Zhang and X. Zhang, *ACS Appl. Mater. Interfaces*, 2015, **7**, 493–503.

58 J. Li, Z. Luo, Y. Zuo, J. Liu, T. Zhang, P. Tang, J. Arbiol, J. Llorca and A. Cabot, *Appl. Catal. B Environ.*, 2018, **234**, 10–18.

59 Y. Gu, J. Luo, Y. Liu, H. Yang, R. Ouyang and Y. Miao, *J. Nanosci. Nanotechnol.*, 2015, **15**, 3743–9.

60 K. D. Gilroy, A. Ruditskiy, H.-C. Peng, D. Qin and Y. Xia, *Chem. Rev.*, 2016, **116**, 10414–10472.

61 P. Strasser, S. Koh, T. Anniyev, J. Greeley, K. More, C. Yu, Z. Liu, S. Kaya, D. Nordlund, H. Ogasawara, M. F. Toney and A. Nilsson, *Nat. Chem.*, 2010, **2**, 454–460.

62 A. Hamza, S. El-Refaei, A. Elzatahry and A. Abdullah, *Appl. Sci.*, 2017, **7**, 64.

63 G. Kresse and J. Furthmüller, *Phys. Rev. B*, 1996, **54**, 11169–11186.

64 G. Kresse and J. Hafner, *Phys. Rev. B*, 1994, **49**, 14251–14269.

65 G. Kresse and J. Hafner, *Phys. Rev. B*, 1993, **47**, 558–561.

66 G. Kresse and J. Furthmüller, *Comput. Mater. Sci.*, 1996, **6**, 15–50.

67 H. Fjellvåg, A. Kjekshus, R. Stomberg, R. Zingales, I. Vikholm, F. Urso, J. Weidlein and R. A. Zingaro, *Acta Chem. Scand.*, 1986, **40a**, 23–30.

68 R. Chang, *General Chemistry: The Essential Concepts*, American Chemical Society, 2006.

69 Y. Liu, X. Liu, Q. Feng, D. He, L. Zhang, C. Lian, R. Shen, G. Zhao, Y. Ji, D. Wang, G. Zhou and Y. Li, *Adv. Mater.*, 2016, **28**, 4747–4754.

70 M. He, L. Protesescu, R. Caputo, F. Krumeich and M. V. Kovalenko, *Chem. Mater.*, 2015, **27**, 635–647.
71 M. Walter, S. Doswald and M. V. Kovalenko, *J. Mater. Chem. A*, 2016, **4**, 7053–7059.
72 M. He, K. Kravchyk, M. Walter and M. V. Kovalenko, *Nano Lett.*, 2014, **14**, 1255–1262.
73 H. G. Meier, J. R. Vilche and A. J. Arvía, *J. Electroanal. Chem. Interfacial Electrochem.*, 1982, **138**, 367–379.
74 E. B. Castro, C. A. Gervasi and J. R. Vilche, *J. Appl. Electrochem.*, 1998, **28**, 835–841.
75 I. G. Casella and M. Gatta, *J. Electroanal. Chem.*, 2002, **534**, 31–38.
76 M. Walter, S. Doswald, F. Krumeich, M. He, R. Widmer, N. P. Stadie and M. V. Kovalenko, *Nanoscale*, 2018, **10**, 3777–3783.
77 M. W. Khalil, M. A. Abdel Rahim, A. Zimmer, H. B. Hassan and R. M. Abdel Hameed, *J. Power Sources*, 2005, **144**, 35–41.
78 L. Wang, G. Zhang, Y. Liu, W. Li, W. Lu and H. Huang, *Nanoscale*, 2016, **8**, 11256–11263.
79 J. Wang, D. Teschner, Y. Yao, X. Huang, M. Willinger, L. Shao and R. Schlögl, *J. Mater. Chem. A*, 2017, **5**, 9946–9951.
80 Y. Yu, Q. Yang, X. Li, M. Guo and J. Hu, *Green Chem.*, 2016, **18**, 2827–2833.
81 D. Chen and S. D. Minteer, *J. Power Sources*, 2015, **284**, 27–37.
82 A. J. Bard and L. R. Faulkner, 2001.
83 D. M. MacArthur, *J. Electrochem. Soc.*, 1970, **117**, 422.

TOC

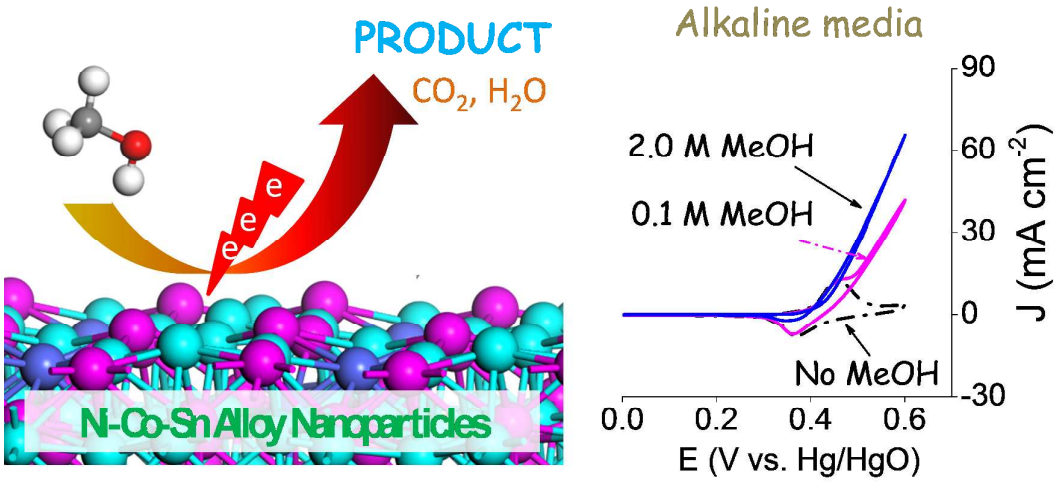

Methanol oxidation reaction in alkaline media and the activity.

Supporting Information

Colloidal Ni-Co-Sn Nanoparticles as Efficient Electrocatalysts for the Methanol Oxidation Reaction

Junshan Li,[a,b] Zhishan Luo,[a,*] Feng He,[c,d,*] Yong Zuo,[a,b] Junfeng Liu,[a,b] Xiaoting Yu,[a,b] Ruifeng Du,[a,b] Ting Zhang,[e] Maria F. Infante-Carrió,[e] Pengyi Tang,[e] Jordi Arbiol,[e,f] Jordi Llorca,[g] Andreu Cabot [a, f,*]

a Catalonia Institute for Energy Research - IREC, Sant Adrià del Besòs, Barcelona, 08930, Spain

b Departament d'Electronica, Universitat de Barcelona, 08028 Barcelona, Spain

c Key Laboratory of Organic Solids, Institute of Chemistry, Chinese Academy of Sciences, Beijing 100190, PR China.

d University of Chinese Academy of Sciences, Beijing 100049, P.R. China.

e Catalan Institute of Nanoscience and Nanotechnology (ICN2), CSIC and BIST, Campus UAB, Bellaterra, 08193 Barcelona, Spain

f ICREA, Pg. Lluís Companys 23, 08010 Barcelona, Spain

g Institute of Energy Technologies, Department of Chemical Engineering and Barcelona Research Center in Multiscale Science and Engineering. Universitat Politècnica de Catalunya, EEBE, 08019 Barcelona, Spain

Corresponding Author

* Andreu Cabot: acabot@irec.cat

* Zhishan luo: luozs@mail.sustc.edu.cn

* Feng He: hefeng2018@iccas.ac.cn

Contents

Additional TEM micrograph

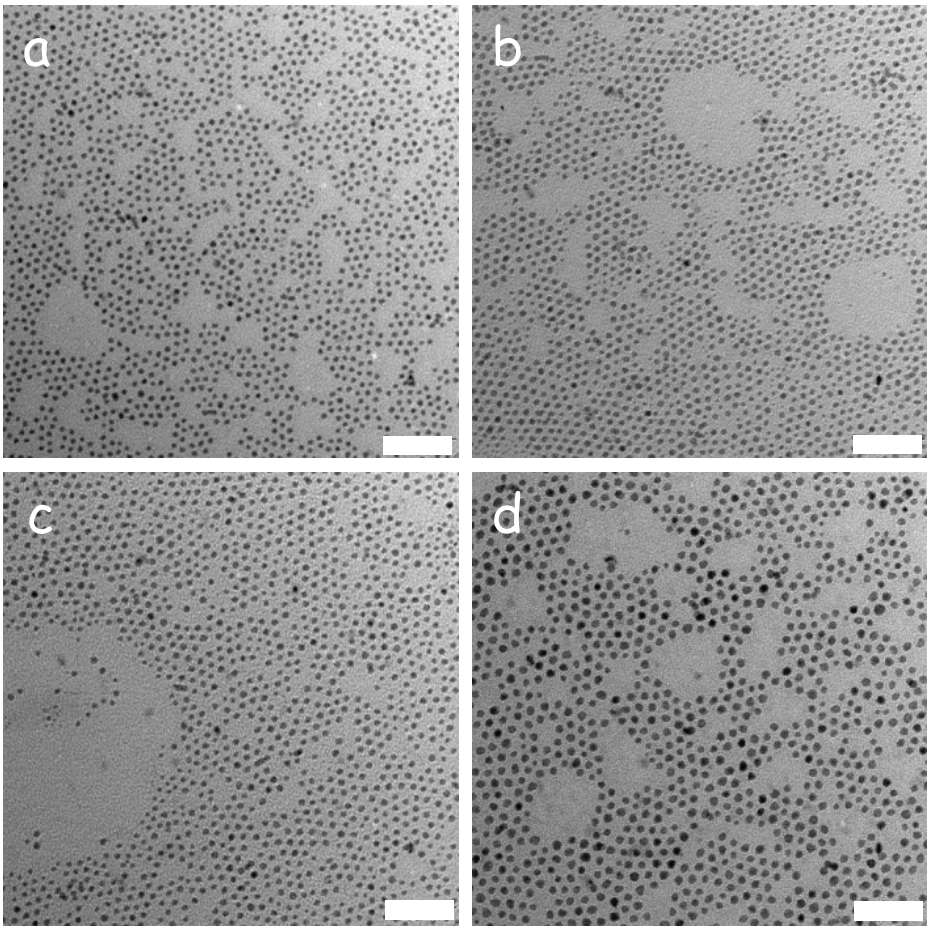

Figure S1. Representative TEM micrographs of $Ni_{3-x}Co_xSn_2$ NPs with different Co contents: a) x = 0.5, b) x = 1.0, c) x = 2.0, d) x = 2.5. Scale bar: 50 nm.

SEM-EDX characterization

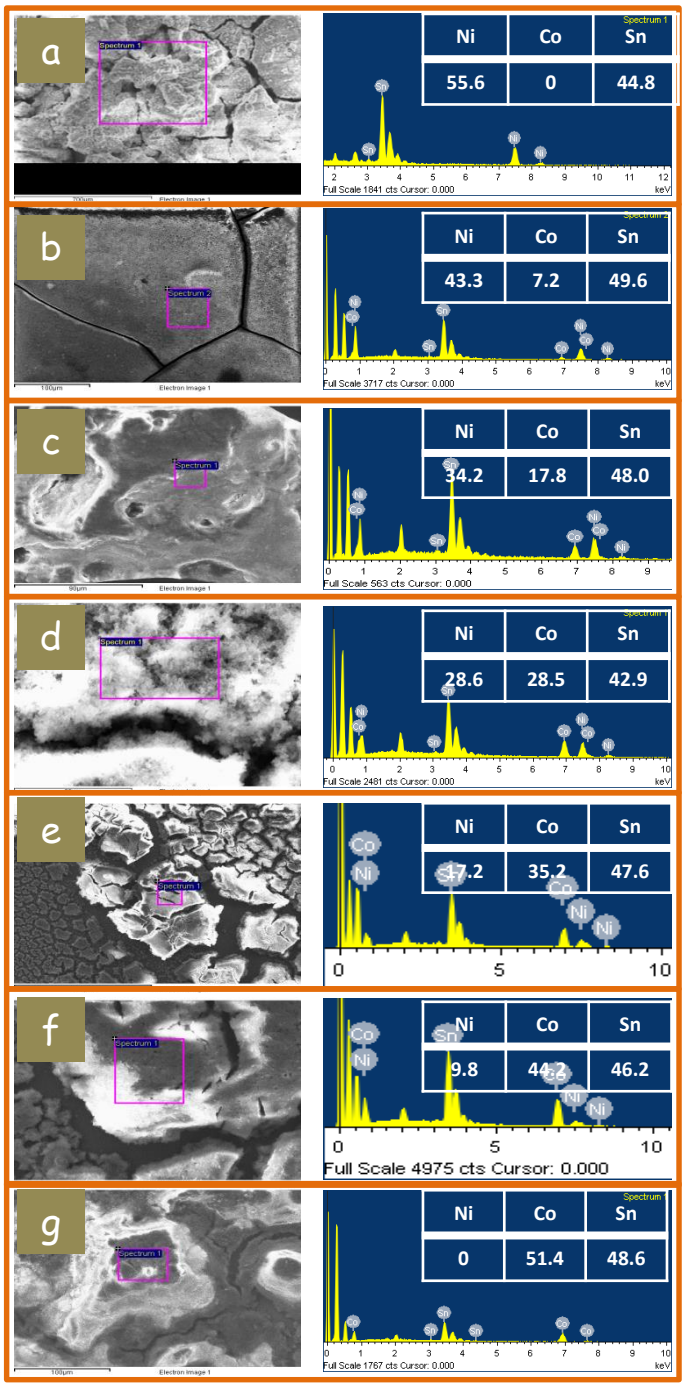

Figure S2. SEM-EDX characterization of the NPs of $Ni_{3-x}Co_xSn_2$: a) x = 0, b) x = 0.5, c) x = 1.0 d) x = 1.5, (e) x = 2.0, f) x = 2.5, g) x = 3.0. In the table, weight percentage for each metal was used.

HRTEM micrographs

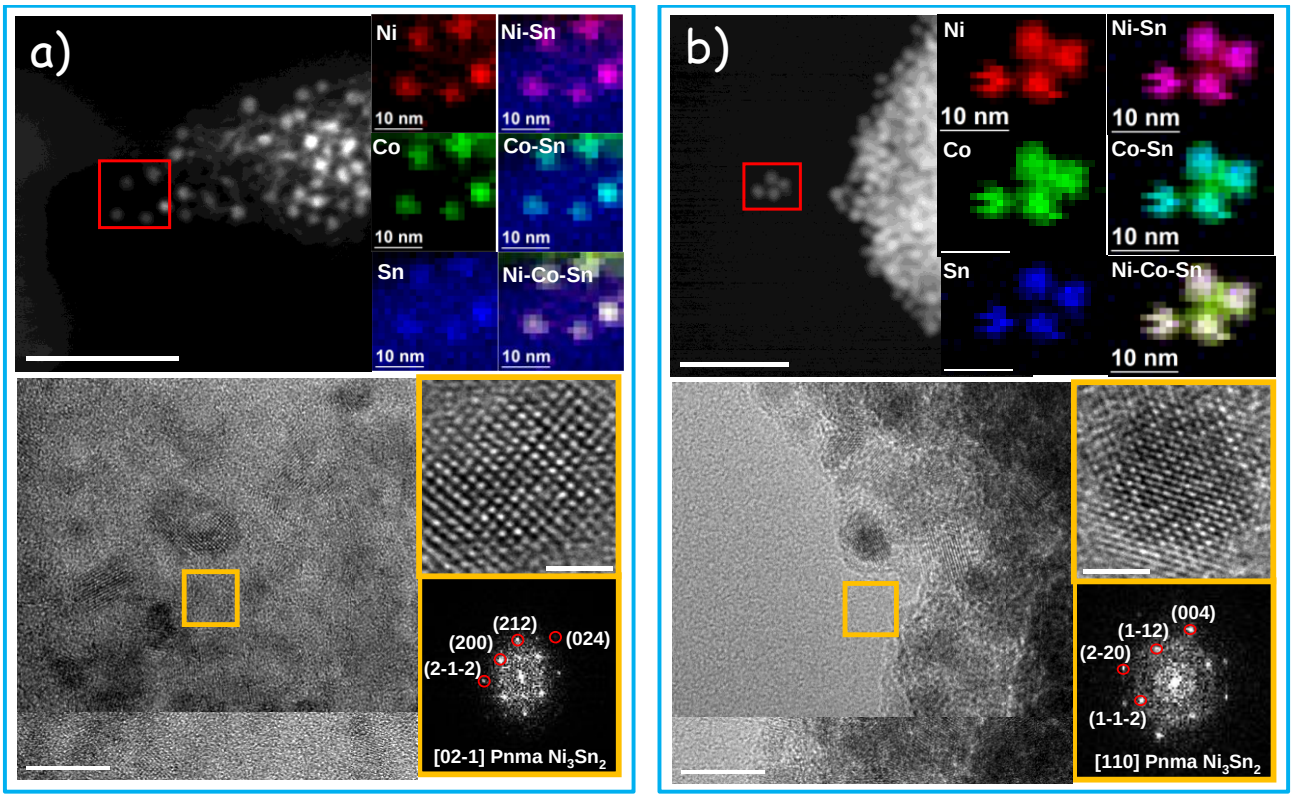

Figure S3. HRTEM micrograph and ADF-STEM image and EELS elemental mapping of $Ni_{3-x}Co_xSn_2$: a) x = 1.0, b) x = 1.5.

XPS characterization

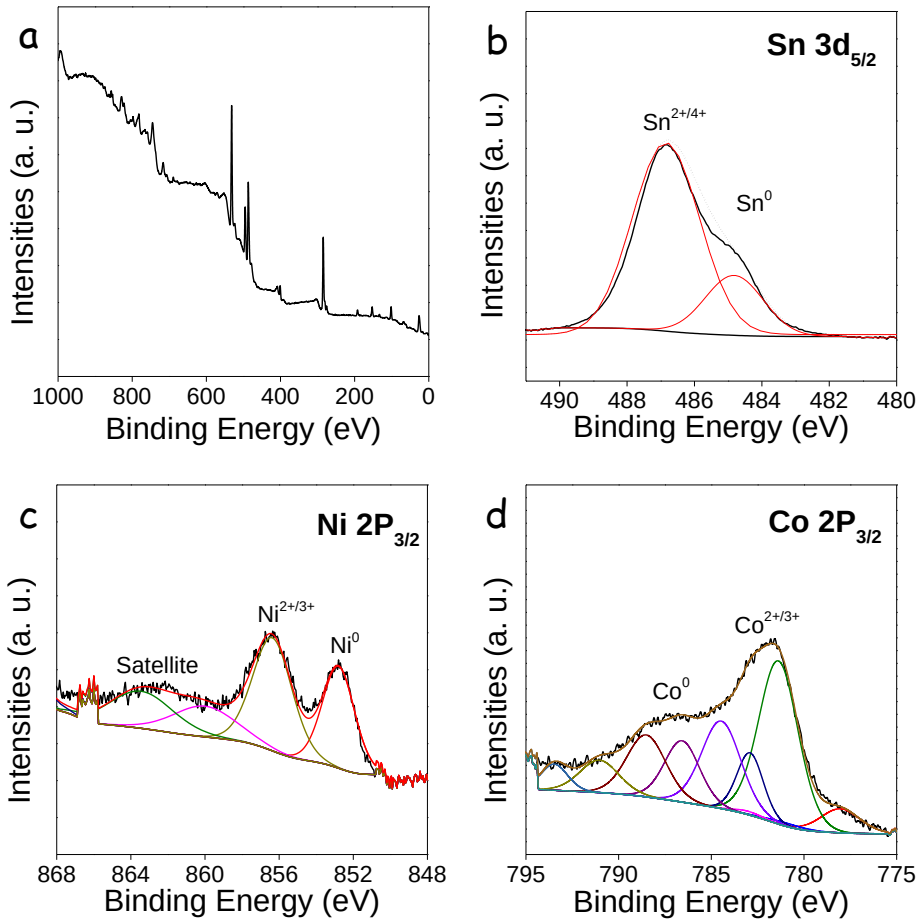

Figure S4. XPS spectra of $Ni_{3-x}Co_xSn_2$ (x = 1.5) NPs.

Ni is presented at the NPs surface in two different chemical states, which we associated to metallic Ni^0 (852.8 eV) and $Ni^{2+/3+}$ chemical environment (856.4 eV).[1] An additional satellite peak was also observed at 863.4 eV. The fitting peaks of 778.0 eV， 781.0 eV and 783.0 eV are indexed to metallic Co and oxides, respectively.[1] The amount of Co^0 is smaller than that of $Co^{2+/3+}$. In addition, two tin chemical states were identified from the XPS analysis of the Sn $3d_{5/2}$ electronic states. A Sn $3d_{5/2}$ peak at higher binding energy, 486.8 eV was assigned to an oxidized environment.[1] A second Sn $3d_{5/2}$ peak at 484.8 eV matched with the binding energy expected from Sn in a metallic environment, thus we related it to the Sn within the $Ni_{3-x}Co_xSn_2$ alloy.[1]

Ligand removal

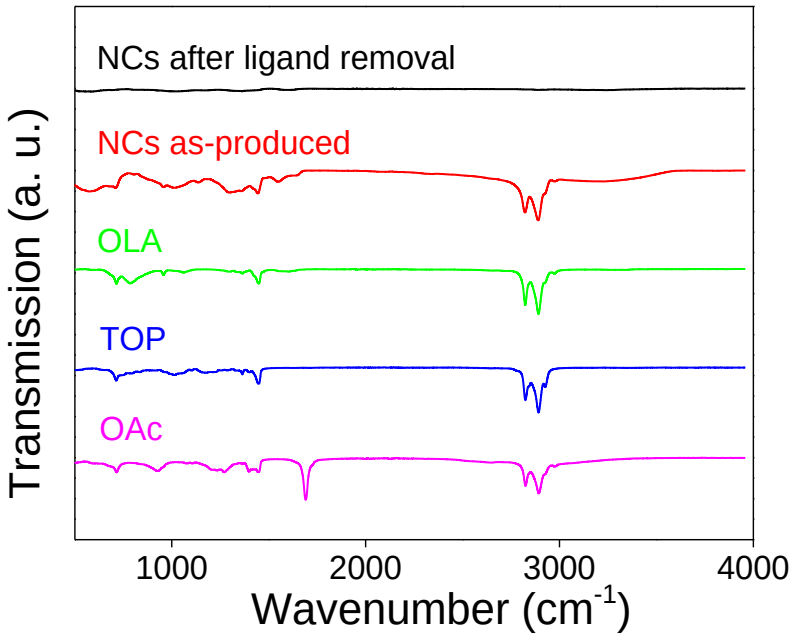

Figure S5. FTIR spectra of OAm, OAc, TOP and $Ni_{3-x}Co_xSn_2$ (x = 0.5) NPs as produced and after ligand removal.

Electrochemical measurements

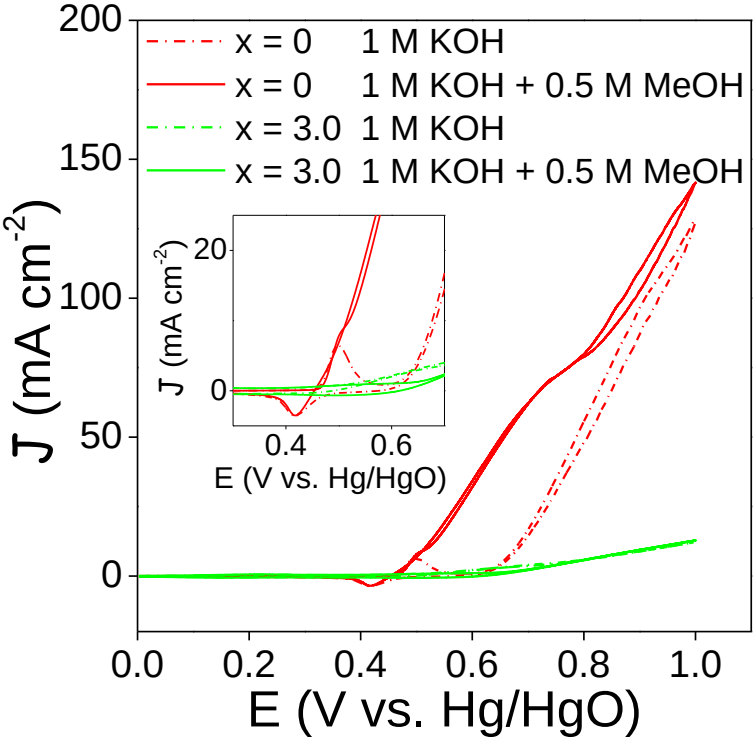

Figure S6. Cyclic voltammograms of $Ni_{3-x}Co_xSn_2$ (x = 0, 3.0) NPs in 1 M KOH solution at a scan rate of 50 mV s^{-1} in the presence and absence of 0.5 M methanol, inset shows an enlarged area of the current density with the applied potential of 0.35-0.65 V.

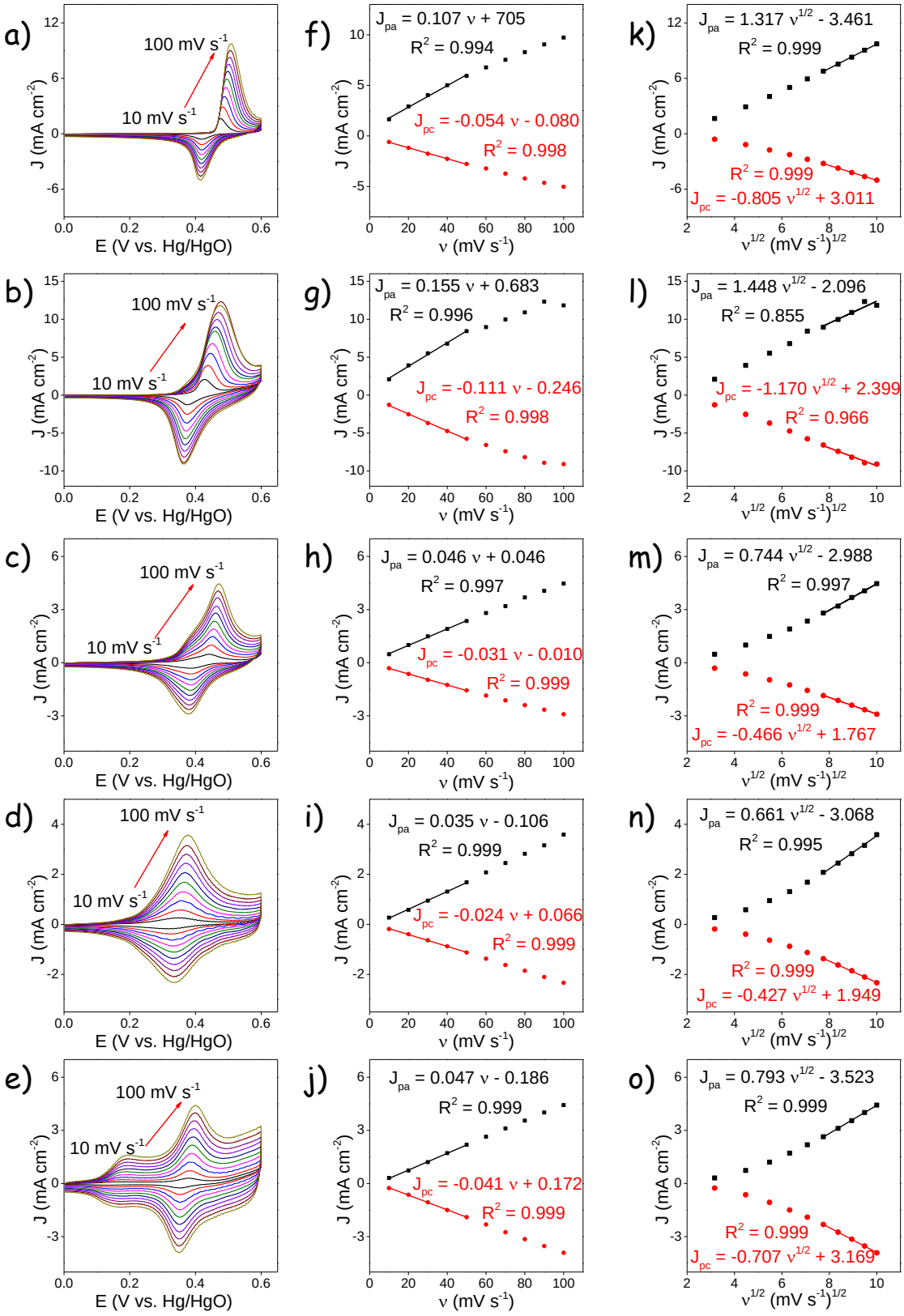

Figure S7. (a-e) Cyclic voltammograms of $Ni_{3-x}Co_xSn_2$ (x = 0, 0.5, 1.0, 2.0, 2.5) NPs in 1 M KOH solution at increasingly higher potentials sweep rates: 10, 20, 30, 40, 50, 60, 70, 80, 90, 100 mVs^{-1}. (f-j) Linear fitting of anodic and cathodic peak current densities to the scan rates of Ni3-xCoxSn2 (x = 0, 0.5, 1.0, 2.0, 2.5) NPs. (k-o)Linear fitting of anodic and cathodic peak current densities to the square roots of the scan rates of $Ni_{3-x}Co_xSn_2$ (x = 0, 0.5, 1.0, 2.0, 2.5) NPs.

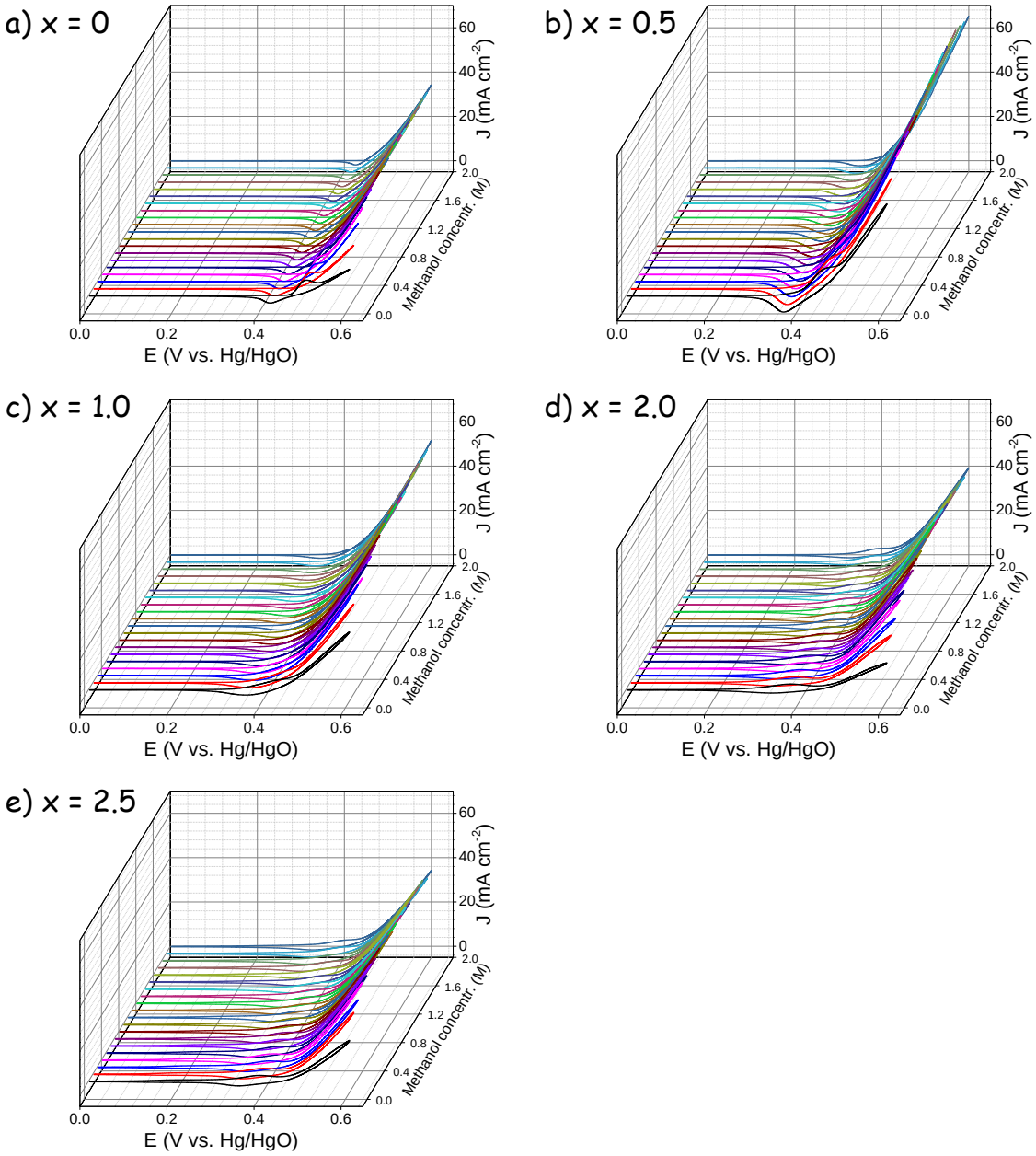

Figure S8. (a-e) CVs of $Ni_{3-x}Co_xSn_2$ (x = 0, 0.5, 1.0, 2.0, 2.5) electrode in 1 M KOH solution with different methanol concentrations from 0.1 M to 2.0 M at a scan rate of 50 mV s^{-1}.

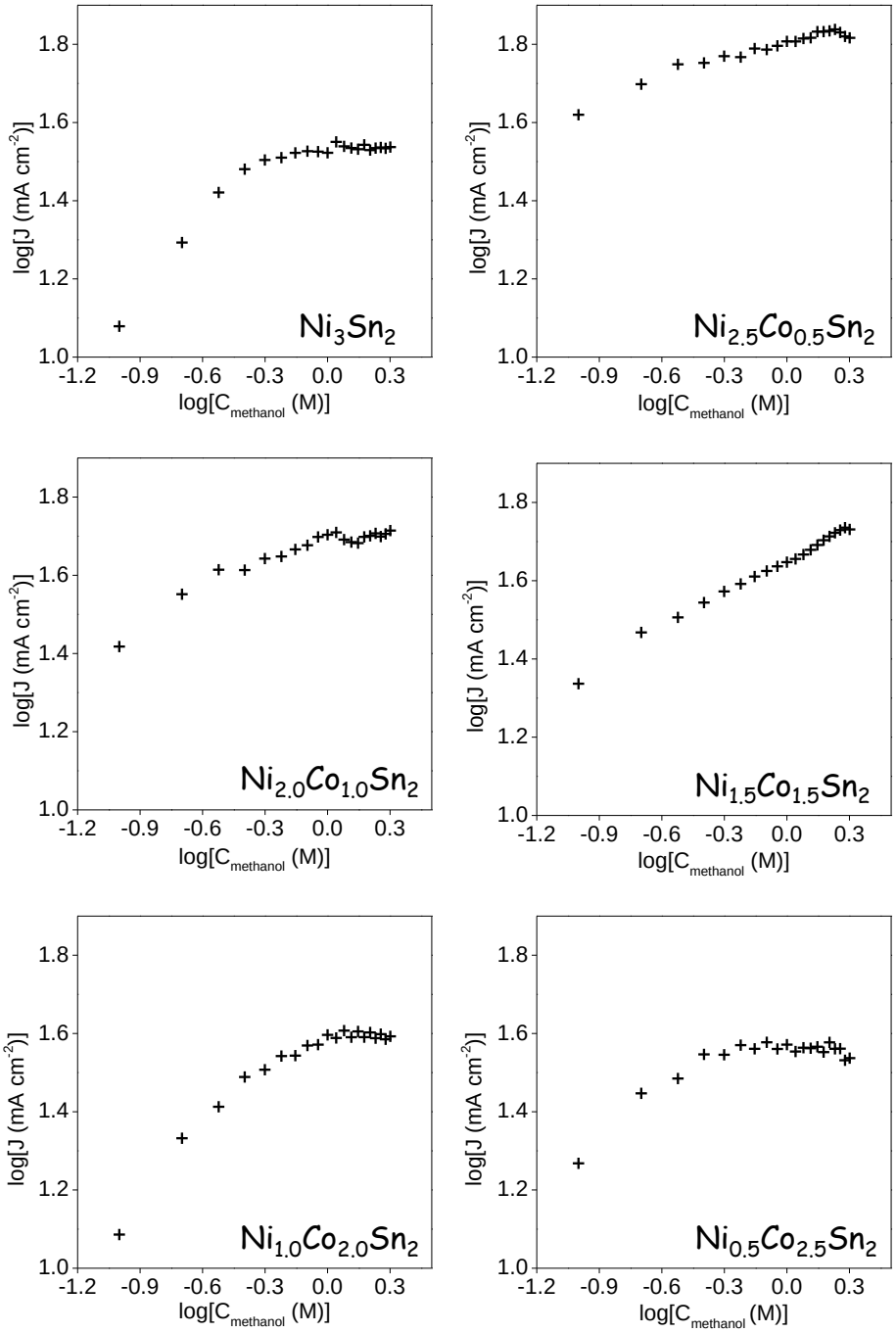

Figure S9. Logarithmic dependence of the current density (0.6 V vs Hg/HgO) for $Ni_{3-x}Co_xSn_2$ ($0 \; x \leq 2.5$) electrode with the methanol concentration in 1 M KOH solution with various methanol concentrations from 0.1 M to 2.0 M.

Computational Details

The calculations were performed using Vienna ab-initio simulation package (VASP).[2–5] The interactions between valence electrons and ion cores were treated by Blöchl's all-electron-like projector augmented wave (PAW) method.[6,7] The exchange-correlation functional was the generalized gradient approximation with the Perdew-Burke-Ernzerhof, known as GGA-PBE.[8] The wave functions at each k-point were expanded with a plane wave basis set and a kinetic cutoff energy up to 400 eV. The electron occupancies were determined according to Fermi scheme with an energy smearing of 0.1 eV. Brillouin zone integration was approximated by a sum over special selected k-points using the Monkhorst–Pack method and they were set to 3×3×1. Geometries were optimized until the energy was converged to 1.0×10^{-6} eV/atom and the force was converged to 0.01 eV/Å. Because of existence the magnetic atom, spin polarization was considered in all calculations. A vacuum layer as large as 20 Å was used along the c direction normal to the surface to avoid periodic interactions.

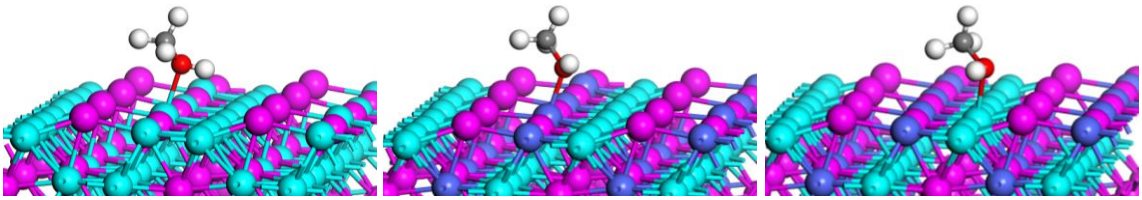

Figure S10. Side view of the absorption of methanol on different atom in (001) surface of Ni_3Sn_2 and $Ni_{2.5}Co_{0.5}Sn_2$ alloy. Green, pink and blue spheres represent Ni, Co and Sn, respectively.

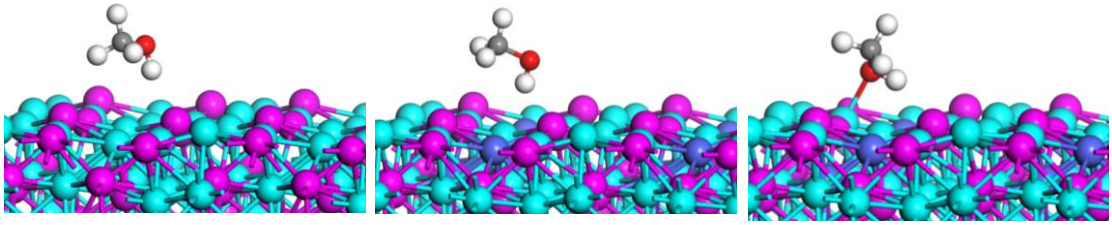

Figure S11. Side view of the absorption of methanol on different atom in (110) surface of Ni_3Sn_2 and $Ni_{2.5}Co_{0.5}Sn_2$ alloy. Green, pink and blue spheres represent Ni, Co and Sn, respectively.

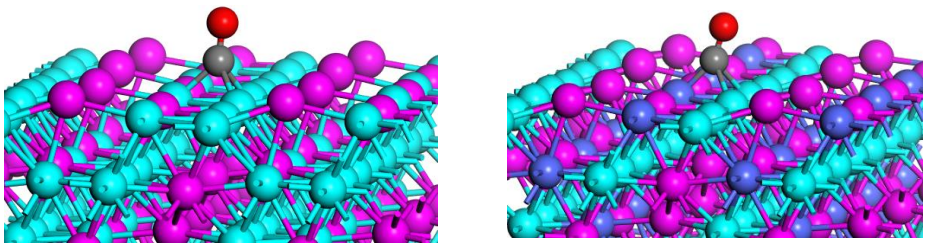

Figure S12. Side view of the absorption of CO in (001) surface of Ni_3Sn_2 and $Ni_{2.5}Co_{0.5}Sn_2$ alloy. Green, pink and blue spheres represent Ni, Co and Sn, respectively.

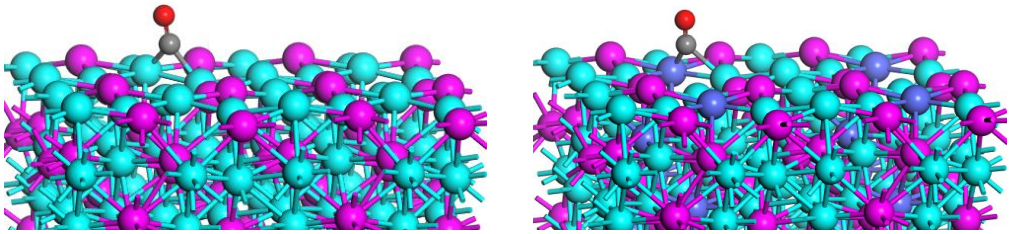

Figure S13. Side view of the absorption of CO in (110) surface of Ni_3Sn_2 and $Ni_{2.5}Co_{0.5}Sn_2$ alloy. Green, pink and blue spheres represent Ni, Co and Sn, respectively.

Comparison of activity

Table S1. Comparison of activity between catalysts in this work and recently reported Ni and Ni-based non-precious metal alloy catalyst

Catalysts	Morphology	Electrolyte	Applied potential❶ V vs. RHE	Activity		Reference
				mA cm^{-2}	mA mg_{metal}^{-1}	
Cu/NiCu/C	Nanowires	1.0 M KOH + 1.0 MeOH	1.55	34.9	867.1	[9]
$Ni_{0.75}Cu_{0.25}$	Branched 3D networks	1 M NaOH + 0.5 MeOH	1.69	45		[10]
Ni	NPs	0.4 M KOH + 1.0 MeOH	1.64	12		[11]
FeNi	NPs	0.1 M NaOH + 1.0 MeOH	1.56	50	1709	[12]
Ni@CNTs	Heterostructures	1.0 M KOH + 1.0 MeOH	1.62	~1.5	966	[13]
Ni_2Co_2	Cauliflower-like	1.0 M NaOH + 0.5 MeOH	1.74	~35		[14]
$Ni_{0.5}Co_{0.5}$	Porous alloy film	1.0 M NaOH + 0.5 MeOH	1.69	~35		[15]
Ni	Ti-supported flakes	1.0 M NaOH + 0.5 MeOH	1.74	39		[16]
Ni-Ti	NPs	0.1 M NaOH + 0.2 MeOH	1.62	0.5 mA		[17]
Ni	NPs@rGO	1.0 M KOH + 1.0 MeOH	1.64		1600	[18]
NiMn	Film	1.0 M NaOH + 0.5 MeOH	1.64	~80		[19]
$Ni_{1.7}Sn$	NPs	0.5 M KOH + 0.5 MeOH	1.65	50.9	819.3	[20]
$Ni_{2.5}Co_{0.5}Sn_2$	NPs	1.0 M KOH + 1.0 MeOH	1.57	65.5	1070.4	This work
Ni_3Sn_2	NPs	1.0 M KOH + 1.0 MeOH	1.57	34.4	562.7	This work
Pt/C*	Commercial	1.0 M KOH + 1.0 MeOH	0.95		710	[9]

Note: *Commercial Pt/C was included here for comparison.

❶ For comparison, the applied potential was intended to convert to be vs. RHE using the following equation:

$$E_{RHE} = E^0_{Ref} + E_{Ref} + 0.059 \times PH$$

Where E^0_{Ref} is potential of the reference ($E^0_{Ag/AgCl} = 0.21$ V, $E^0_{Hg/HgO} = 0.14$ V), E_{Ref} is the potential that measured vs. reference, PH is simply converted from the electrolyte ($PH = 14 + \lg[OH^-]$, $[OH^-]$ is the OH^- concentration of the alkaline media).

Reference

1 C. D. Wager, W. M. Riggs, L. E. Davis, J. F. Moulder and G. E. Muilenderg, *Handbook of X-ray photoelectron spectroscopy*, Perkin-Elmer Corporation Physical Electronics Division, 1979.

2 G. Kresse and J. Furthmüller, *Phys. Rev. B*, 1996, **54**, 11169–11186.

3 G. Kresse and J. Hafner, *Phys. Rev. B*, 1994, **49**, 14251–14269.

4 G. Kresse and J. Hafner, *Phys. Rev. B*, 1993, **47**, 558–561.

5 G. Kresse and J. Furthmüller, *Comput. Mater. Sci.*, 1996, **6**, 15–50.

6 P. E. Blöchl, *Phys. Rev. B*, 1994, **50**, 17953–17979.

7 G. Kresse and D. Joubert, *Phys. Rev. B*, 1999, **59**, 1758–1775.

8 J. P. Perdew, K. Burke and M. Ernzerhof, *Phys. Rev. Lett.*, 1996, **77**, 3865–3868.

9 D. Wu, W. Zhang and D. Cheng, *ACS Appl. Mater. Interfaces*, 2017, **9**, 19843–19851.

10 X. Cui, P. Xiao, J. Wang, M. Zhou, W. Guo, Y. Yang, Y. He, Z. Wang, Y. Yang, Y. Zhang and Z. Lin, *Angew. Chemie Int. Ed.*, 2017, **56**, 4488–4493.

11 R. M. Abdel Hameed and R. M. El-Sherif, *Appl. Catal. B Environ.*, 2015, **162**, 217–226.

12 S. L. Candelaria, N. M. Bedford, T. J. Woehl, N. S. Rentz, A. R. Showalter, S. Pylypenko, B. A. Bunker, S. Lee, B. Reinhart, Y. Ren, S. P. Ertem, E. B. Coughlin, N. A. Sather, J. L. Horan, A. M. Herring and L. F. Greenlee, *ACS Catal.*, 2017, **7**, 365–379.

13 J. Wang, D. Teschner, Y. Yao, X. Huang, M. Willinger, L. Shao and R. Schlögl, *J. Mater. Chem. A*, 2017, **5**, 9946–9951.

14 X. Cui, W. Guo, M. Zhou, Y. Yang, Y. Li, P. Xiao, Y. Zhang and X. Zhang, *ACS Appl. Mater. Interfaces*, 2015, **7**, 493–503.

15 X. Cui, Y. Yang, Y. Li, F. Liu, H. Peng, Y. Zhang and P. Xiao, *J. Electrochem. Soc.*, 2015, **162**, F1415–F1424.

16 Q. Yi, W. Huang, J. Zhang, X. Liu and L. Li, *Catal. Commun.*, 2008, **9**, 2053–2058.

17 Y. Yu, Q. Yang, X. Li, M. Guo and J. Hu, *Green Chem.*, 2016, **18**, 2827–2833.

18 H. Sun, Y. Ye, J. Liu, Z. Tian, Y. Cai, P. Li and C. Liang, *Chem. Commun.*, 2018, **54**, 1563–1566.

19 I. Danaee, M. Jafarian, A. Mirzapoor, F. Gobal and M. G. Mahjani, *Electrochim. Acta*, 2010, **55**, 2093–2100.

20 J. Li, Z. Luo, Y. Zuo, J. Liu, T. Zhang, P. Tang, J. Arbiol, J. Llorca and A. Cabot, *Appl. Catal. B Environ.*, 2018, **234**, 10–18.